PNNL-25981

Pacific Northwest
NATIONAL LABORATORY
Proudly Operated by Battelle Since 1965

Active Time-Domain Reflectometry for Unattended Safeguards Systems: FY16 Report

October 2016

JR Tedeschi
LE Smith
RC Conrad
G Gavric
M Zalavadia
D Keller
R Pratt

U.S. DEPARTMENT OF
ENERGY

Prepared for the U.S. Department of Energy
under Contract DE-AC05-76RL01830

PACIFIC NORTHWEST NATIONAL LABORATORY
operated by
BATTELLE
for the
UNITED STATES DEPARTMENT OF ENERGY
under Contract DE-AC05-76RL01830

Printed in the United States of America

Available to DOE and DOE contractors from the
Office of Scientific and Technical Information,
P.O. Box 62, Oak Ridge, TN 37831-0062;
ph: (865) 576-8401
fax: (865) 576-5728
email: reports@adonis.osti.gov

Available to the public from the National Technical Information Service,
U.S. Department of Commerce, 5285 Port Royal Rd., Springfield, VA 22161
ph: (800) 553-6847
fax: (703) 605-6900
email: orders@ntis.fedworld.gov
online ordering: http://www.ntis.gov/ordering.htm

This document was printed on recycled paper.
(9/2003)

PNNL-25981

Active Time-Domain Reflectometry for Unattended Safeguards Systems: FY16 Report

JR Tedeschi
LE Smith
RC Conrad
G Gavric
M Zalavadia
D Keller
R Pratt

October 2016

Prepared for
the U.S. Department of Energy
under Contract DE-AC05-76RL01830

Pacific Northwest National Laboratory
Richland, Washington 99352

Abstract

The International Atomic Energy Agency (IAEA) continues to expand its use of unattended measurement systems. An increasing number of systems and an expanding family of instruments create challenges in terms of deployment efficiency and the implementation of data authentication measures. Traditional data security measures, for example tamper-indicating (TI) conduit, are impractical for the long separation distances (often 100 meters or more) between unattended monitoring system (UMS) components. Pacific Northwest National Laboratory (PNNL) is studying the viability of active time-domain reflectometry (TDR) for the detection of cable tampering in unattended radiation detection systems. The instrument concept under investigation would allow for unmanned cable integrity measurements, remote surveillance reporting and locating of cable faults and/or tampers. This report describes PNNL's FY16 progress and includes: an overview of the TDR methods under investigation; description of the TDR evaluation testbed developed by PNNL; development and testing of advanced signal processing algorithms to extract weak signals from relatively high noise levels; and initial testing of a laboratory prototype intended for IAEA UMS applications and based on a commercially available TDR module. Preliminary viability findings and recommendations for the next stage of development and testing are provided.

Acknowledgments

This research was supported by the U.S. National Nuclear Security Administration (NNSA) Office of Nonproliferation and Arms Control (NA-24), Office of International Nuclear Safeguards, under Contract DE-AC05-76RL01830 with the U.S. Department of Energy. Pacific Northwest National Laboratory is a multi-program national laboratory operated by Battelle for the U.S. Department of Energy.

The authors would like to thank Roman Simlinger and Cesare Liguori of the IAEA for their collaboration on LiveWire implementation options.

We also very much appreciate Mitch Anderson, Brent Waddoups and Lucas Thomson from LiveWire for their technical support on the Mantis system.

Acronyms and Abbreviations

ASIC	application specific integrated circuit
BPSK	binary phase shift keyed
COTS	commercial off-the-shelf
DAQ	data acquisition
DC	direct current
DSSS	direct sequence spread spectrum
DUT	device under test
EMI	electromagnetic interference
FAR	false alarm rate
FDR	frequency domain reflectometry
FEE	front-end electronics
FEUM	front-end electronics for unattended measurement
FFT	fast Fourier transform
FWHM	full-width at half-maximum
GUI	graphical user interface
HPF	high pass filter
IAEA	International Atomic Energy Agency
LPF	low pass filter
MCA	multi-channel analyzer
PCB	printed circuit board
PD	probability of detection
PNNL	Pacific Northwest National Laboratory
PTFE	polytetrafluoroethylene
RF	radio-frequency
ROC	receiver operating characteristic
SFTDR	swept-frequency time domain reflectometry
SMA	sub-miniature version A
SNR	signal-to-noise ratio
SSH	secure shell
SSTDR	spread-spectrum time domain reflectometry
TDR	time domain reflectometry
TI	tamper-indicating
TTL	transistor-transistor logic
UMS	unattended monitoring system
VNA	vector network analyzer
VPN	virtual private network

Contents

Figures

Tables

1.0 Introduction

Remotely monitored, unattended nondestructive assay systems are central to the IAEA's ability to safeguard an expanding global fuel cycle with limited manpower and financial resources. As the number of unattended monitoring instruments increases, the IAEA is challenged to become more efficient in the implementation of those systems, and to ensure the authenticity of data coming from an expanding family of instruments. Unfortunately, traditional data security measures, for example tamper-indicating (TI) conduit, are impractical for the long separation distances (often 100 meters or more) between unattended monitoring system (UMS) components. Challenges include the fact that such conduit requires detailed physical inspection by the IAEA during on-site visits, and often, the cabling is routed through multiple penetrations in difficult-to-access parts of the facility. The need for new TI options is identified in the IAEA Department of Safeguards Long-Term R&D Plan, 2012-2023: "ability to communicate secure, authentic information…between the IAEA…and equipment in the field" [1]. Figure 1 below illustrates how a new TI analysis capability might be integrated in a nominal UMS instrument fielded by the IAEA.

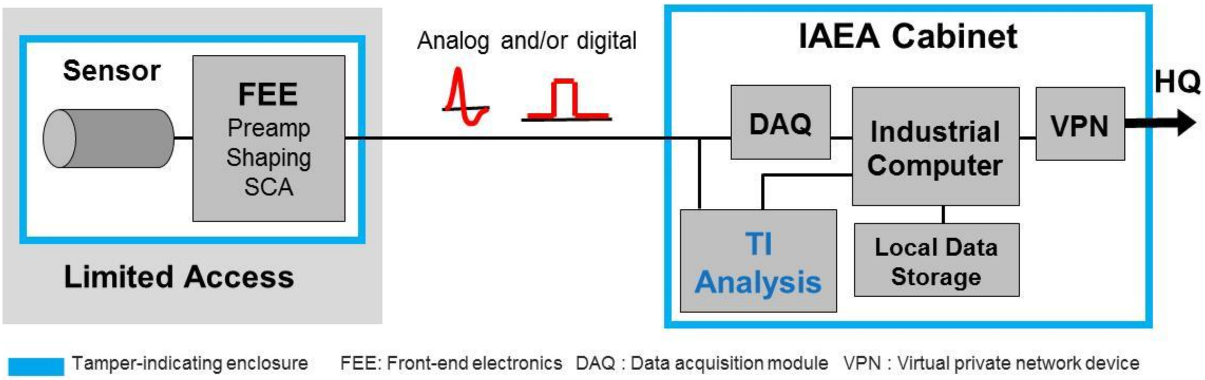

Figure 1. Conceptual depiction of how a new tamper-indication (TI) analysis method might be integrated in an IAEA unattended monitoring system, which includes front-end electronics (FEE), data acquisition (DAQ) components, and secure communications via a virtual private network (VPN).

Time domain reflectometry (TDR) is a promising candidate technology to address IAEA's tamper-indication challenges because of its proven success in cable measurement and analytics. The signal transmitted by the TDR instrument travels down the cable being monitored, reflects from impedance changes within the cable, and the reflected signal is received by the TDR instrument. The received signal is then compared to a reference of the transmitted signal, and this comparison provides active TDR relatively high gain, good noise immunity, and the ability to localize tampers. Important for IAEA radiation detector instrumentation, active TDR signals can, in principle, be tuned to avoid interference with the radiation sensor signals being transmitted on the cabling.

The active-TDR concept for IAEA's unattended radiation detection systems assumes continuous, autonomous monitoring of multiple cables (via multiplexing from a single TDR module). Characterization of the cables to be monitored, to detect any off-normal features in the as-installed cabling and to define the reference baseline TDR signals for each cable, will be performed at deployment.

The appropriate scanning parameters and alarm thresholds will then be configured (e.g., based on cable length and type) for continuous monitoring.

In this project, PNNL is performing a viability study of a candidate TI method for IAEA's unattended radiation detection systems. Preliminary functional requirements and representative scenarios have been developed, in collaboration with the IAEA, to guide the study [2]. Cable-tampering scenarios include taps, splices, disconnects, and replacements, with a focus on the tap scenario. Metrics for evaluation of the candidate TI methods include detection probability and false-alarm rate under various operational conditions, ability to localize the tampering event, and diagnostic information that could aid the IAEA in determining the likely cause of the tamper indication.

The key outcomes from this three-year project (October 2015 through September 2018) are:

1) Development of a prototype tamper-indication module based on the spread-spectrum TDR (SSTDR) technology implemented in LiveWire's Mantis, augmented with software and hardware tailored to the specific needs of IAEA use cases.
2) Performance assessment of the prototype device for representative tamper scenarios and using metrics appropriate for long-term monitoring with IAEA's unattended systems.
3) Field demonstration of a field-ready prototype tamper-indication module that is designed for integration into a nominal IAEA unattended radiation detection architecture.

This report describes PNNL's FY16 progress against these objectives, and includes: descriptions of the IAEA use cases that guide the study; an overview of the TDR methods considered in this work; PNNL's benchtop testbed for evaluating the performance of candidate TDR methods; development of signal-processing algorithms tailored to detecting of physical tampering in UMS cabling; and preliminary performance results using a COTS-based laboratory prototype. Recommended next steps in the viability study are also described.

2.0 Background

From its inception, PNNL's study of candidate TDR methods has been focused on the detection of physical intrusion into the cabling. To date, the IAEA has not issued formal requirements for new technologies designed to detect physical tampering in UMS cabling. Absent formal requirements, PNNL is referencing the preliminary functional requirements and performance targets defined by multiple organizations (including PNNL, Los Alamos National Laboratory and Idaho National Laboratory) [2]. Cable tampering scenarios defined in that document include taps, splices, disconnects, and replacements. Metrics for evaluation of the candidate TI methods include detection probability and false-alarm rate under various operational conditions, ability to localize the tampering event, and the value of diagnostics provided by each method that could aid the IAEA in determining the likely cause of the tamper indication. It is assumed that the primary role of the TI method is to raise a flag that indicates the instrumentation system may have been compromised and, therefore, that safeguards data produced by that instrument from that time forward may be suspect. As described in [2], two use cases, representative of IAEA UMS deployments today and the in the future, guide this viability study:

Use Case 1: Retrofit of advanced TI methods into existing deployments where the sensor is co-located with the front-end electronics (FEE) (Figure 2). This is the highest priority use case because it is how the vast majority of IAEA systems are deployed today. Use Case 1 has been the focus of PNNL's TDR investigation to date.

Use Case 2: Integration of advanced TI methods in deployments where the FEE is separated from the sensor, creating two distinct sections of cabling, one between the sensor and the FEE, and the other between the FEE and the IAEA cabinet (Figure 3). Use Case 2 may be addressed in future work but is not discussed further in this FY16 annual report.

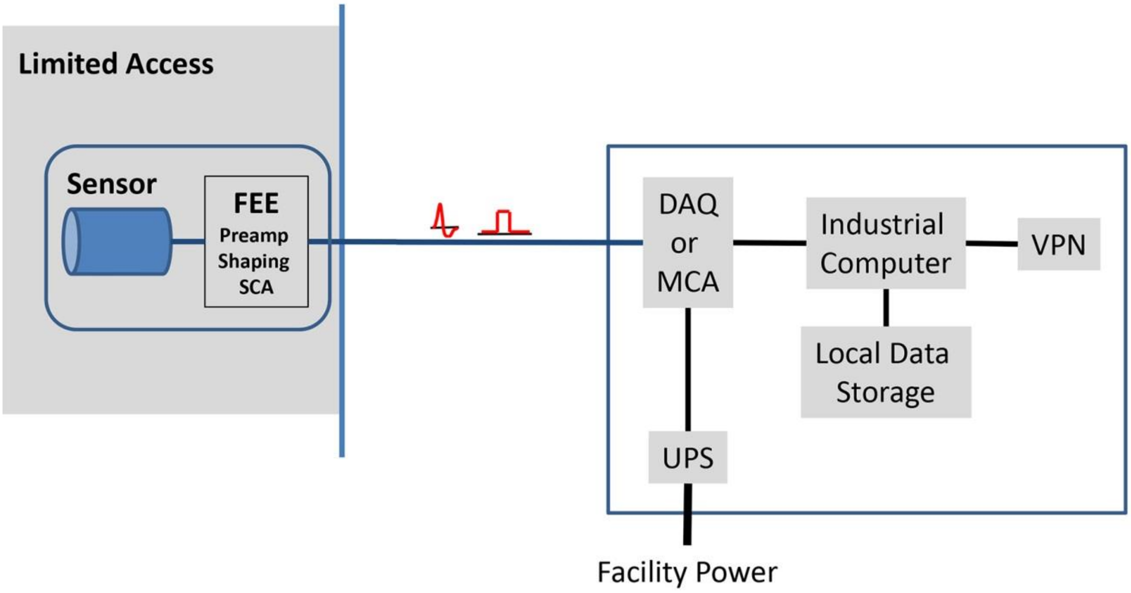

Figure 2. Use Case 1, FEEs are co-located with the sensors, often inside an area of limited personnel access.

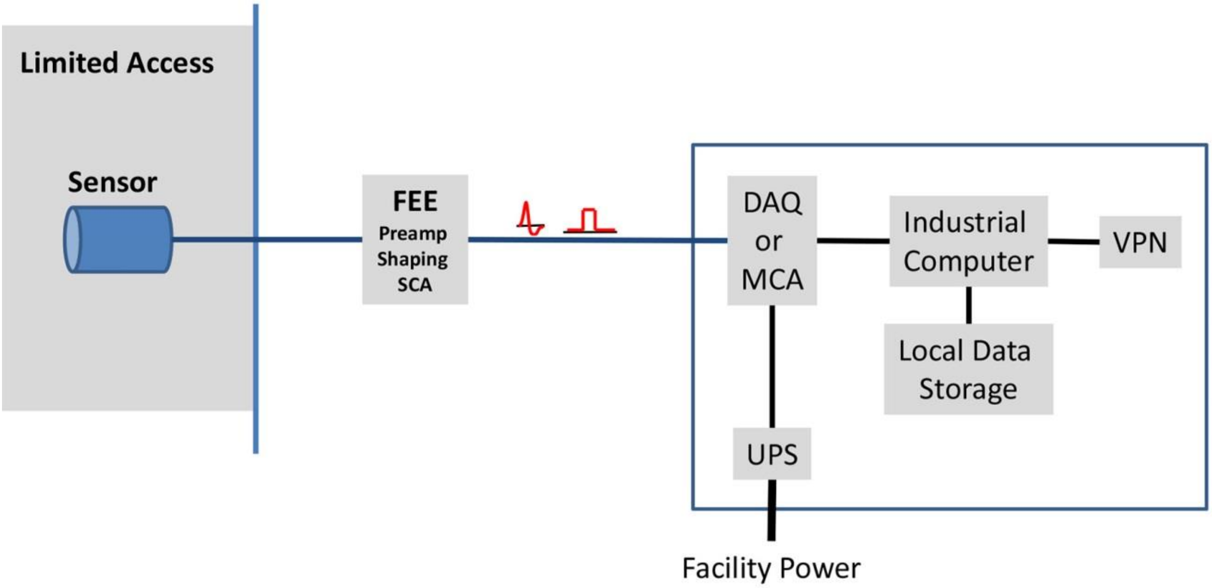

Figure 3. Use Case 2, FEEs are separated from the sensor and the cabinet.

It is assumed in this study that the baseline, unperturbed condition of the cabling is verified and known upon initial installation of the UMS cabling and equipment so that TI methods for physical intrusion are focused on detecting *changes* in the cabling characteristics from that baseline. Note that while these use cases are illustrated above with a single sensor and FEE, typical IAEA deployments involve multiple sensors and multiple cables.

This goal of this study is to illuminate the strengths and limitations of the LiveWire SSTDR method for the IAEA UMS application, using the tampering scenarios and performance metrics defined previously. The key technical questions to address over this multi-year study include:

- Can SSTDR signals be distinct/separable from the frequency spectra of UMS sensors?
- How effectively can candidate methods (hardware + algorithms) detect tampering scenarios?
- How might a TDR-based device interface with common IAEA data acquisition systems?
- Are there obvious vulnerabilities in the methods and, if so, how might they be addressed?

3.0 TDR Methods: Overview

PNNL's initial investigation of the viability of TDR for the detection of physical intrusion into cabling includes swept-frequency TDR (SFTDR) as the highly flexible, laboratory gold standard to which field-deployable options can be compared, and LiveWire's SSTDR technology as one option for field implementation. A brief description of each is provided below.

3.1 Swept-Frequency Time-Domain Reflectometry

The SFTDR measurement, also termed frequency domain reflectometry (FDR), method is put to practice in this study using an Keysight Technologies Vector Network Analyzer (VNA). The VNA TDR technique uses Fourier analysis of swept frequency domain signals, velocity of signal propagation, and transmission line impedance changes to determine both amplitude and position in time/space of reflected signals. Figure 4 below shows the VNA highlighting port 1 where the cable under test will be connected for the TDR measurements.

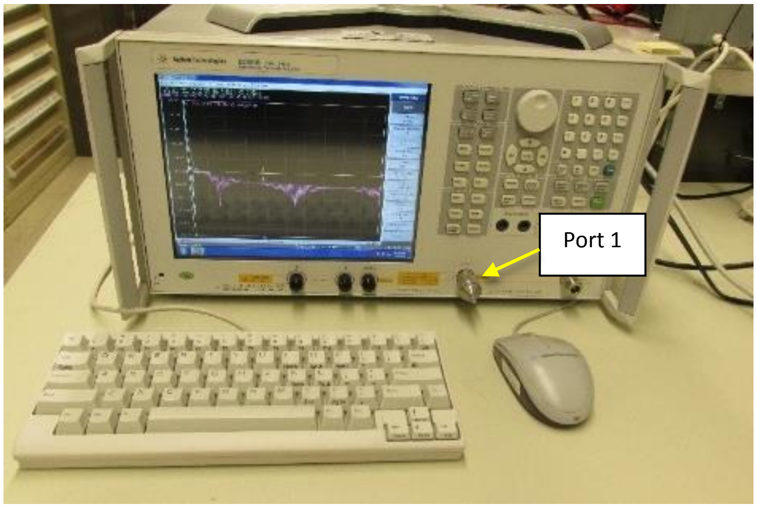

Figure 4. Keysight Technologies VNA.

For a standard coaxial transmission line, the line impedance is expected to be nominally continuous throughout the cable; however, if the cable now connects to a device under test (DUT), there will be a reflection if the DUT impedance does not perfectly match the impedance of the coaxial line. The reflection coefficient is defined as follows:

$$\rho = \frac{Z_{DUT} - Z_0}{Z_{DUT} + Z_0},$$

where Z_0 is the transmission line impedance and Z_{DUT} is the impedance of the DUT. Performing an electronic calibration on the VNA [3] corrects for the insertion loss, impedance, and phase associated with the VNA and its test cables that connect the VNA to the DUT. Therefore, this allows the VNA to perform fully calibrated amplitude and phase frequency measurements that are in response to the DUT.

The VNA then performs a swept frequency domain reflection measurement and mathematically computes a time domain transform using the chirp-Z Fast Fourier Transform technique [4]. The reflection or S11 measurement refers to the measured signal amplitude and phase received at Port 1 relative to the transmitted amplitude and phase from Port 1. The time domain data is then converted into the spatial domain by a second translation using signal phase velocity, also expressed as the velocity of light in the medium. The phase velocity for non-magnetic materials is determined using the equation shown below [5],

$$v_P = \frac{c}{\sqrt{\varepsilon_r}}$$

where c is the speed of light (3×10^8 m/s), and ε_r is the real part of the dielectric constant of the propagation medium. For reference, the phase velocity in polyethylene and polytetrafluoroethylene (PTFE), are 66% and 69% of the phase velocity in free space respectively.

3.2 Spread-Spectrum TDR with LiveWire’s Mantis

SSTDR-LiveWire [6] was designed to operate continually in the background of a system to monitor for cable breaks and shorts without influencing the operation of the system being monitoring. LiveWire uses a spread spectrum TDR (SSTDR) technique with low-power signals that, when viewed in the frequency domain, appear as noise rather than continuous wave or swept continuous wave signals. For SSTDR to generate its ‘noise’ frequency range, a sine wave that has been shaped into a square wave is multiplied by a pseudo noise correlator; this generates a direct sequence spread spectrum (DSSS) binary phase shift keyed (BPSK) signal [7]. This DSSS BPSK signal is then mixed with the original sine wave to produce a spread-frequency spectrum signal that is injected into the cable. Figure 5 presents an example of a sine wave being BPSK modulated.

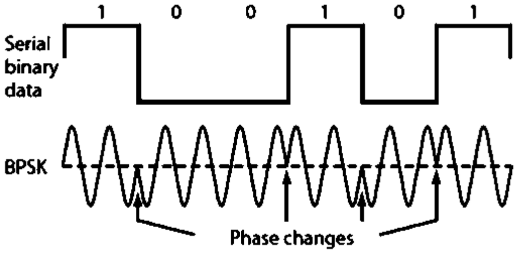

Figure 5. Sine wave BPSK modulated signal time domain response.

The return signal, after reflection from discontinuities in the transmission path, includes any added noise or other frequency content (e.g., from radiation-sensor signals) from the system being monitored. The reference signal is the original sine wave with a variable phase delay applied; adjusting the phase delay allows for localization of the discontinuities in the cable. The reflected signal is cross-correlated with a reference signal to determine the location of the discontinuity. The amplitude of the cross correlation result is based on the overlap between the reference signal and the detected signal. Noise or other signals present on the cable will not correlate well to the reference and thus will have a small amplitude, whereas a reflected signal from an impedance discontinuity will overlap well with the reference signal and create a large amplitude. Figure 6 below shows an example correlation result where there is poor overlap between a reference signal and the detected signal except for the time equating to 100 meters from the transmitting end of the cable. At this point in time the received signal correlated well to the reference and has a large signal response compared to all other points in time.

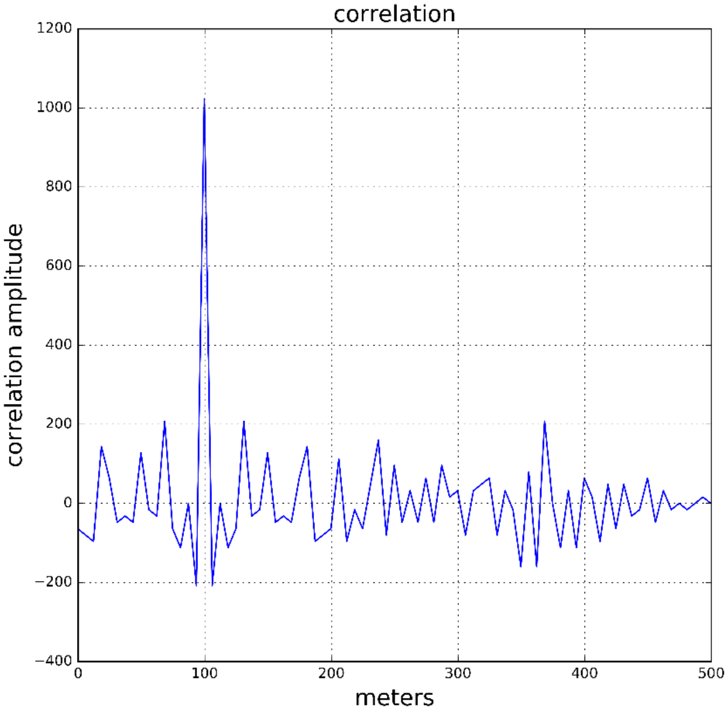

Figure 6. Cross correlation example result.

In 2010, the IAEA began an investigation of the LiveWire TDR method for applicability in both surveillance and unattended radiation detection systems. The very early proof-of-concept tests performed by the IAEA and a LiveWire representative were encouraging but inconclusive. The IAEA continued its study of LiveWire with a focus on surveillance applications using analog cameras (e.g., radiation-hardened cameras). IAEA staff purchased a LiveWire ASIC, designed and fabricated printed circuit boards (PCBs) to support the ASIC and the accompanying microcontroller, and developed a software interface to support testing. By 2013, those tests were sufficiently successful to support a dedicated integration effort for IAEA surveillance needs. A project under the German Support Program to the IAEA has now been completed to integrate the LiveWire ASIC in the controller module for one of the IAEA analog camera systems.(a)

While the IAEA's study of LiveWire for surveillance has proceeded significantly in recent years, to the authors' knowledge there has been no corresponding progress on its viability for unattended radiation detection systems. The PNNL work described in this report is intended to address this need, and PNNL appreciated the support and sample implementation (i.e., PCB and software used by the IAEA to explore the LiveWire ASIC). As described in PNNL's FY15 annual report for the NA-241 project that preceded the current project, the IAEA's prior work focused on surveillance systems was highly useful to PNNL's initial investigation of the ASIC for unattended radiation detection systems [8].

(a) Martin Moeslinger, International Atomic Energy Agency, personal communication, 2016.

While the LiveWire ASIC was the focus of PNNL's initial investigation of COTS SSTDR, LiveWire informed PNNL in early FY16 that the SSTDR ASIC would be phased out of production and therefore, LiveWire would no longer be selling or supporting the device. (The IAEA purchased a large supply of the ASIC to ensure that their analog surveillance needs can be met for the foreseeable future.) LiveWire also shared that they had developed a new ruggedized SSTDR instrument termed Mantis (Figure 7) designed for monitoring cable continuity/integrity. The Mantis system is battery-powered, and provides communication of impedance discontinuities via Wi-Fi or email. The Mantis system is designed to operate at a higher level than the ASIC that PNNL tested prior to FY16. That is, users control the Mantis system through a graphical user interface (GUI), but the number of TDR parameters available to the user for tuning is somewhat reduced compared to the ASIC.

Figure 7. LiveWire Innovations' Mantis SSTDR instrument package. Mantis functionality is also available in a board-stack form.

PNNL acquired a Mantis system during the 1st quarter of FY16 and to provide continuity with prior study of the ASIC-based SSTDR implementation, PNNL performed some comparative performance studies (described later in this report). Once it was confirmed that the SSDTR functionality and performance Mantis was equivalent to that of the ASIC, PNNL's measurement studies with the ASIC were discontinued, and Mantis became the sole focus of the viability study.

4.0 Evaluation Testbed: Overview

PNNL's TDR evaluation testbed is depicted in Figure 8 below. It is intended to emulate a nominal IAEA UMS configuration, and includes an instrument rack (analogous to the IAEA UMS cabinet in Figure 1) as well as cables of varying lengths and types extended from the DAQ cabinet to the FEE. As in Use Case 1 described previously, the detector is adjacent to the FEE. A 3-port interface is designed to connect the radiation sensor to the TDR system and to the data acquisition modules for the UMS detector signals, in this case Amptek's MCA8000D multi-channel analyzer (MCA), often referred to as the Pocket MCA. The 3-port interface allows simultaneous collection of radiation-detector signals by the Pocket MCA and SSTDR signals by the TDR system. (The development details of the 3-port interface are discussed later in the report.) PNNL's modular testbed provides the ability to modify the parameters of the TDR and radiation-sensor components, and to perform the parameters studies described in the sections that follow.

In FY16, a NaI(Tl) (hereafter, "NaI") gamma-ray spectrometer (Ludlum model 44-2, 2.5x2.5cm cylinder, nominal energy resolution of ~11% at 662 keV, operating voltage of 800 volts, shaping time 2.0 µs.) was used as a representative UMS sensor. Note that this detector was primarily manufactured for the purpose of gross counting, and not for spectroscopic measurements. Hence, the detector construction and photo-multiplier tube selection is not well suited to achieve the best possible energy resolution for a NaI sensor. NaI was chosen as the first UMS sensor type to study for several reasons, including single-cable operation (i.e., the anode signal is superimposed on the high-voltage provided by the FEE) typical of many IAEA UMS installations, and a relatively high pulse amplitude (due to multiplication of scintillation light with a photomultiplier tube). The latter characteristic was deemed a suitable starting point for studies on whether UMS sensors interfere with Mantis signals, and vice versa. Future work will evaluate Mantis performance in conjunction with other UMS sensor types and signals, for example ^{3}He neutron detectors, TTL signals, fission chambers and current-mode ion chambers.

A 13.4 µCi ^{137}Cs source was used in the FY16 studies described in this report. Placed very near the face of the NaI spectrometer, a count rate of ~17 kcps is produced with a lower discriminator setting of ~57 keV. Lower count rates were achieved by increasing the distance between source and detector. It should be noted that this as-tested count rate is significantly lower than is often encountered in UMS applications (500 kcps is not unusual) and therefore, the full effect of interference between UMS sensors and Mantis may not be yet understood. Future work will more fully investigate the effect of count rate interference.

The FEE package utilized in PNNL's FY16 measurement studies was one of the prototype Front-End for Unattended Measurement (FEUM) units developed by Bot Engineering and previously tested by PNNL against IAEA user requirements [9][10]. The FEUM module consists of an integrated high-voltage power supply, pre-amplifier and a shaping amplifier. The shaping times associated with the amplifier are user selectable via selection of dip switches. The analog output from the FEUM is routed to an MCA via the power divider. Other COTS FEE options, including other types deployed by the IAEA UMS Team, could be considered in future work. In some cases, the FEE package must be chosen based on the UMS sensor under investigation (e.g., ion chambers coupled to an ammeter data acquisition system).

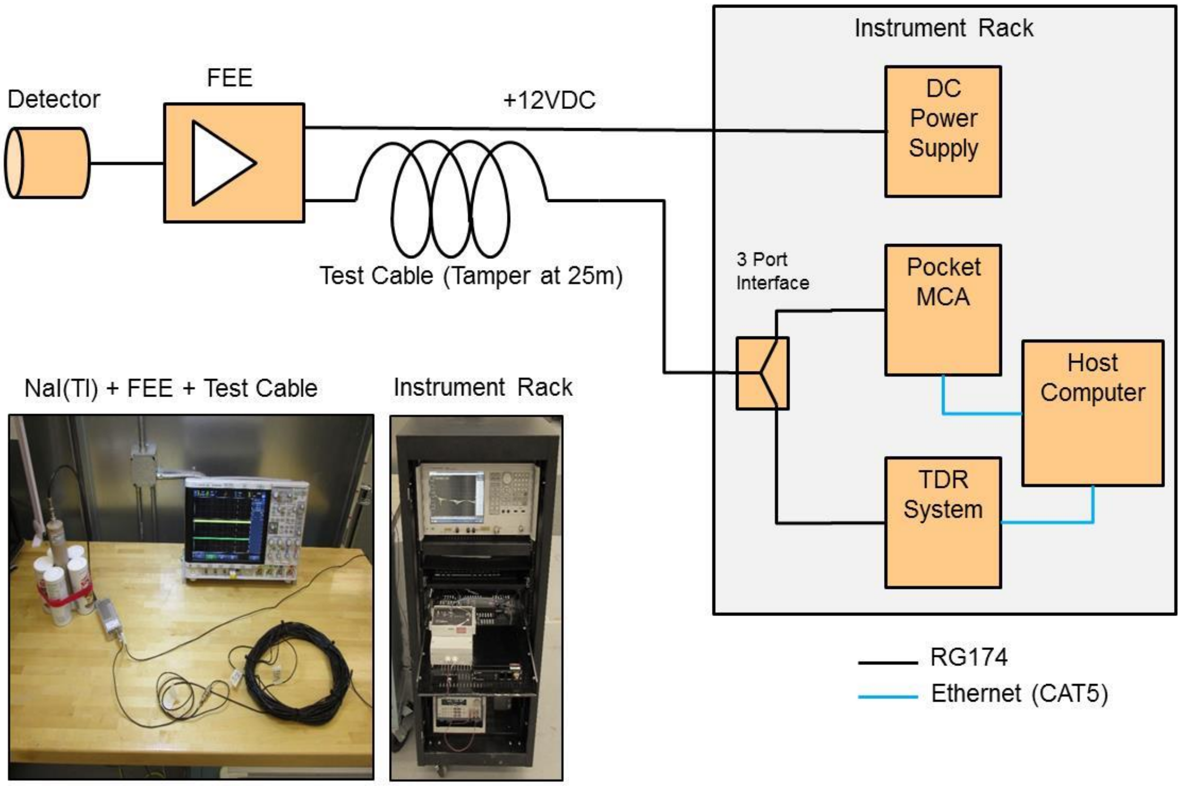

Figure 8. PNNL's TDR test configuration.

The test cable shown in Figure 8, which was used to generate the results presented in this report, is a 50-m RG174 coaxial cable (50-ohm characteristic impedance). RG-174 has been used to support the studies to date, while noting that other cable types (e.g., RG-71) are often used in IAEA UMS installations. Consideration of other cable types is a subject of future work. To emulate a physical tampering scenario, small penetrations were cut into the cable outer conductor at various distances along the cable, which allowed for insertion of an oscilloscope probe (10 Mohm) to contact the center conductor. Figure 9 below shows an example of a cut in the cable outer conductor at nominally 2mm x 2mm in size. This cut provides enough room for the probe to make contact with the center conductor of the cable without shorting to the cable ground (outer conductor), which would cause a very large impedance change. The ground reference for the probe then made contact with the outer conductor of the cable. The validity of the probe placement, to emulate a tap-like tamper, was confirmed by observing radiation detector pulses on the oscilloscope.

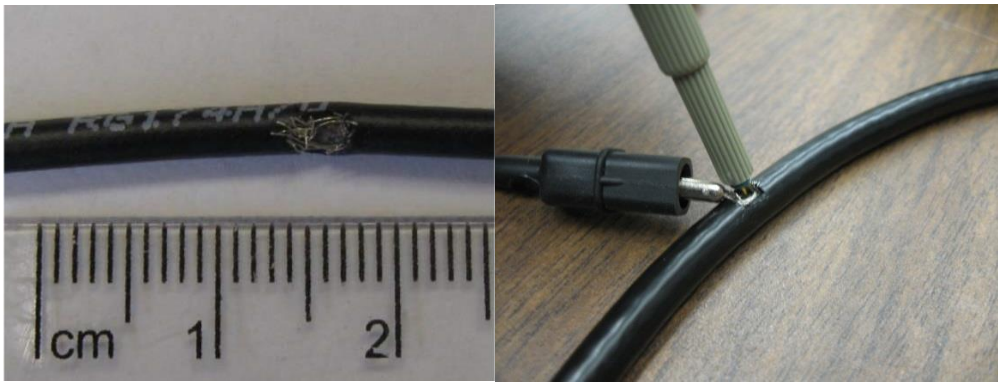

Figure 9. Cable tampering cut (left) and tamper insertion (right) examples.

The physical tamper with the oscilloscope probe can be observed as a high impedance in parallel with the 50-ohm characteristic impedance of the cable, and therefore the effective impedance change is essentially negligible.

$$R_1 \parallel R_2 = \frac{R_1 R_2}{R_1 + R_2} \rightarrow \frac{10e6 * 50}{10e6 + 50} \approx 49.9998\Omega$$

The magnitude of the reflected signal is proportional to the change in impedance:

$$S_{11} = 20\log_{10}\left(\frac{Z_0 - Z_{DUT}}{Z_0 + Z_{DUT}}\right) \rightarrow 20\log_{10}\left(\frac{50 - 49.9998}{50 + 49.9998}\right) \approx \text{-114 dB}$$

Not surprisingly, the -114 dB (which corresponds to 0.0000000004% of the energy transmitted being reflected back) is an extremely small amount of energy and nearly undetectable using TDR methods. However, the presence of a physical tamper produces an additional deformation to the ideal 50-Ohm structure of the cable which is due to the change in physical parameters of the cable (diameter, dielectric material, conductor separation, etc.). This deformation generates a larger impedance change than the electrical impedance of the high impedance probe, and it is this perturbation that is being detection by the Mantis system.

Every cable type has its own transmission loss vs. frequency curve, but a common trend is that as the frequency of the transmitted signal increases, so does the loss. That is why for extremely long cables (kilometers), relatively low TDR frequencies in the KHz range are used. On the other hand, high frequencies and wide bandwidths are used to provide sharp down-range resolution and eliminate blind spots that can happen at close ranges due to initial impedance discontinuities between the TDR system and the cable under test. Generally speaking, the amplitude of the SSTDR correlation signal decreases as the tampers get farther away from the Mantis system, at a rate of approximately two times the cable transmission loss since the Mantis signals are going out and back.

5.0 Purpose-built Software for Tamper Indication

While the Mantis is a promising hardware platform for the implementation of TDR for IAEA applications, the vendor's data acquisition and analysis software is not well-aligned with IAEA use cases. For example, the high-level GUI described above, that provides only limited control of the SSTDR parameters and no access to the raw data, created a challenge for the PNNL team in terms of researching and tuning Mantis's performance in a laboratory setting. In addition, the Mantis analysis and alarming algorithms are designed specifically for detection of cable breaks and short circuits, which are very large impedance changes of interest to the majority of their end users, but are not the entirety of IAEA concerns. The IAEA is also interested in physical tampers on coaxial cables that produce much smaller impedance changes which can conceivably be buried in system noise. Having the ability to work with the Mantis raw data, and to apply advanced signal processing algorithms to extract weak signals in relative strong backgrounds, is critical to this viability study.

The various software modules developed by PNNL to date are described in the sections that follow. They include modules for control of Mantis parameters and acquisition of raw SSTDR data, data reduction and visualization, advanced signal processing to extract weak signals, alarming algorithms, and performance evaluation. Important to note is that all of the PNNL-developed software is nonproprietary and to the extent possible, developed using common scientific programming language (i.e., Python).

5.1 Mantis Control and Raw Data Acquisition

As noted above, Mantis was not initially configured to provide raw SSTDR waveforms needed for the viability analysis that is the foundation of this project. Fortunately, LiveWire provided helpful support in developing algorithms to extract the raw data from the Mantis system, and also provided PNNL the ability to have more control over the measurement parameters.

Putty, a free and open-source terminal emulator that is often used for serial console and network file transfers, was used to make a secure shell (SSH) connection to Mantis (Figure 10). This provided PNNL access to control settings for the SSTDR waveform that are not available at the Mantis standard GUI interface. Scans were initiated using Putty and the raw data was saved locally onto to the Mantis system. Once the scans are complete and saved, they were transferred to a computer using an open source Windows Secure Copy (WinSCP) program. Because Mantis does not currently support real-time data streaming, these same steps would need to be taken in order to transfer and process the data in a field-prototype system connected to an IAEA UMS data acquisition computer. It should be noted, however, that LiveWire communicated initial interest in developing real-time data streaming for the Mantis system. PNNL will continue to inquire about this possibility.

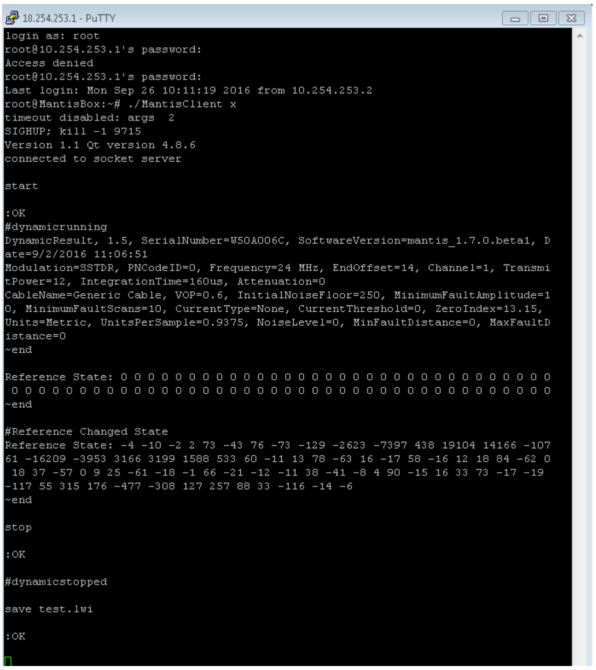

```
login as: root
root@10.254.253.1's password:
Access denied
root@10.254.253.1's password:
Last login: Mon Sep 26 10:11:19 2016 from 10.254.253.2
root@MantisBox:~# ./MantisClient x
timeout disabled: args  2
SIGHUP; kill -1 9715
Version 1.1 Qt version 4.8.6
connected to socket server

start

:OK
#dynamicrunning
DynamicResult, 1.5, SerialNumber=W50A006C, SoftwareVersion=mantis_1.7.0.beta1, D
ate=9/2/2016 11:06:51
Modulation=SSTDR, PNCodeID=0, Frequency=24 MHz, EndOffset=14, Channel=1, Transmi
tPower=12, IntegrationTime=160us, Attenuation=0
CableName=Generic Cable, VOP=0.6, InitialNoiseFloor=250, MinimumFaultAmplitude=1
0, MinimumFaultScans=10, CurrentType=None, CurrentThreshold=0, ZeroIndex=13.15,
Units=Metric, UnitsPerSample=0.9375, NoiseLevel=0, MinFaultDistance=0, MaxFaultD
istance=0
~end

Reference State: 0 0 0 0 0 0 0 0 0 0 0 0 0 0 0 0 0 0 0 0 0 0 0 0 0 0 0 0 0 0 0 0
 0 0 0 0 0 0 0 0 0 0 0 0 0 0 0 0 0 0 0 0 0 0 0 0 0 0 0 0 0 0 0 0 0 0 0 0 0 0 0 0
~end

#Reference Changed State
Reference State: -4 -10 -2 2 73 -43 76 -73 -129 -2623 -7397 438 19104 14166 -107
61 -16209 -3953 3166 3199 1588 533 60 -11 13 78 -63 16 -17 58 -16 12 18 84 -62 0
 18 37 -57 0 9 25 -61 -18 -1 66 -21 -12 -11 38 -41 -8 4 90 -15 16 33 73 -17 -19
-117 55 315 176 -477 -308 127 257 88 33 -116 -14 -6
~end

stop

:OK

#dynamicstopped

save test.lwi

:OK
```

Figure 10. Putty software interface to Mantis, implemented via command prompt.

5.2 Data Formatting and Visualization

After the Mantis raw data is collected on the analysis computer, the challenge becomes displaying the data in a meaningful way that helps highlight the effects of different signal processing techniques. The raw Mantis data format is in a .lwi file format that includes scan header information (date, SSTDR frequency, distance sampling, units, etc.) and the SSTDR amplitude response at every distance sample. This can easily be imported into computational software; Python Spyder was used for this effort. A single scan can be viewed in the data set as correlation amplitude (y-axis) vs. distance (x-axis), which is the typical view for the SSTDR data display on Mantis. Generally speaking, Mantis collects approximately 10,000 scans per minute under the parameter settings used by PNNL to date. To better visualize this large volume of data in a way that highlights the time evolution of tampers, a matrix format has been defined in which the row index corresponds to the start time of a given scan; the column index corresponds to distance (or time within a single scan); and the color in the image corresponds to the signal amplitude. Figure 11 below illustrates how a single scan view (left pane) is incorporated into a matrix image (right pane) showing approximately 10 minutes of data.

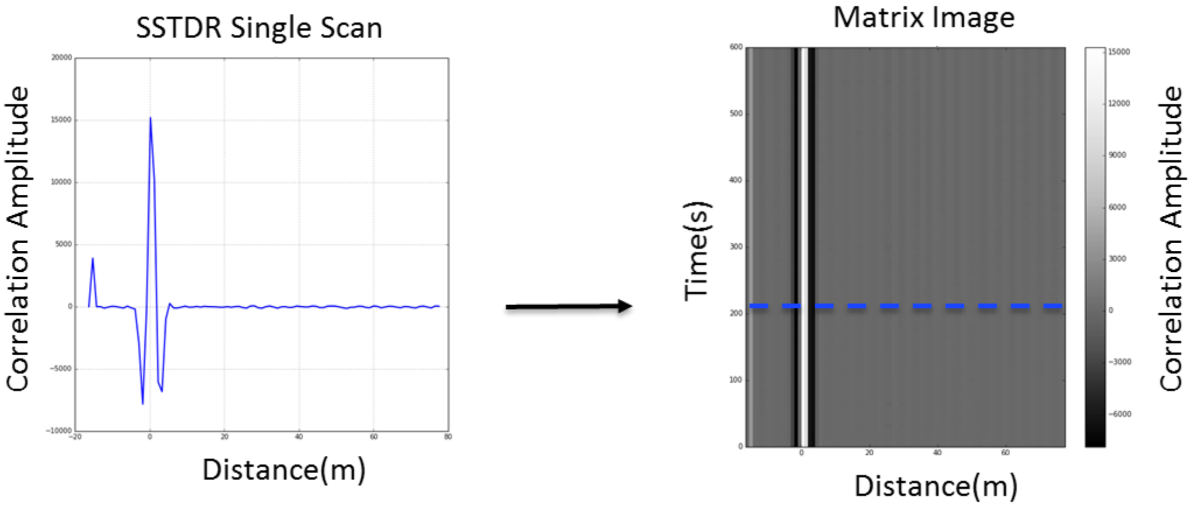

Figure 11. SSTDR data visualization for a single scan (left) and 10 minutes of scans in matrix image (right).

The matrix image display is the standard view adopted by PNNL in the discussion of signal processing and performance evaluation.

5.3 Signal processing Algorithms

The Mantis system is designed for industry, railways and power transmission lines, looking for large impedance changes due to cable breaks, and short/open circuits. Since the Mantis system is optimized for these specific applications, the out-of-the-box Mantis analysis and alarming algorithms are not able to accurately detect the more difficult cases of tampering by taps and splices. Scoping studies verified that Mantis' standard thresholding and detection metrics were not sensitive enough to distinguish these small impedance changes from the drift and noise in the correlation amplitude response. PNNL, therefore, began development and testing of various candidate signal processing techniques intended to detect weak tamper signals from the relatively high background signals likely to be encountered in IAEA UMS applications.

To begin the investigation of potential signal processing techniques for Mantis raw data, a program was created in Python to generate simulated SSTDR scans. This program is capable of generating synthetic raw data sets that can then be analyzed using signal processing techniques of various combinations and parameters. Some of the signal characteristics applied to the synthetic Mantis data, to emulate systematic and random perturbations expected in field operation, are described here:

- sinusoidal trend within each row (i.e., across the distance dimension) to represent potential undulating structure in the Mantis correlation response;
- sinusoidal trend in each column (i.e., across the scan start time dimension) to represent periodic drifting in the amplitude of the Mantis transmitted signal from scan to scan;
- linear amplitude drift over time in the column dimension;
- phase drift in the row dimension to be representative of temperature fluctuations;

- Gaussian noise;
- Artifact having similar characteristics to the response observed from a physical tamper with Mantis.

Example synthetic Mantis data is depicted in the figures supporting the discussion of candidate signal processing algorithms below. It should be noted that a number of potential algorithms were explored preliminarily (including baseline subtraction, signature correlation, spline fitting, walking – baseline subtraction, and thresholding based upon complex signal magnitude derived from a Hilbert transform of the real SSTDR data). Three methods were selected for additional study: median polish, average scan reduction, and fast Fourier transform filtering. An overview of each and examples of how they have been applied to the synthetic Mantis data, are provided here. These three techniques are noted for their ability to achieve the two primary processing challenges in the Mantis data: 1) removing the common-mode signal that is nominally present in every scan, and 2) eliminate random noise that in theory, changes with every scan.

5.3.1 Median Polish

Common mode signal can be removed by a baseline subtraction, but this simple method is susceptible to system drift over time and must be refreshed in order to ensure the drift of the system has not exceeded the sensitivity level required to isolate a tamper. Therefore, a technique called median polish [11], often employed in machine learning to remove common trends in data sets, has been explored. The removal of the common trends in a data set leave non-continuous / periodic features termed residuals. It was hypothesized that the nominal correlation structure present in every scan, and amplitude drift in the Mantis system, could be removed by employing median polish. The implementation of the median polish algorithm was a processing loop defined in Python. The loop would determine the median value in each row and remove it, followed by the median value in each column and remove it. The resulting matrix would then be compared to its previous state, if they were different then the loop would iterate again, but if the matrices were the same to within numerical precision of the calculations, then the matrix was said to have converged to a stable state and the processing loop would exit.

Figure 12 below shows a matrix image of synthetic Mantis data that has sinusoidal trends in both the x and y dimension, but no Gaussian noise (left pane). A simulated tamper event was inserted in the lower right quadrant of the matrix. For this kind of data set, standard baseline subtraction will fail due to the two sinusoidal trends that have both constructive and destructive interference. (If a baseline is removed it will simply create new sinusoidal trends with inverted amplitudes.) The median polish, however, effectively iterates to remove the median values in both the x and y dimensions, and removes the common trends. The simulated tamper event becomes much more clearly distinguishable in the residual values of the process data (right pane).

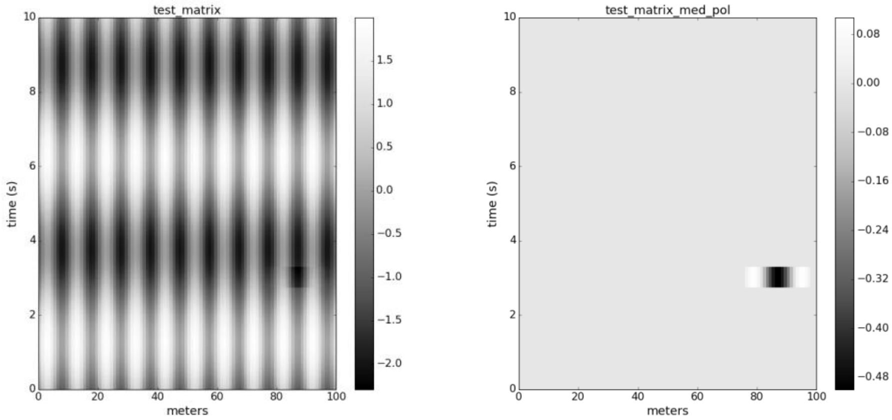

Figure 12. Simulated Mantis raw data matrix (left) with sinusoidal trends in both the row and column dimensions, and a simulated tamper in lower right quadrant of the matrix. Processed data, post median polish, improves the contrast of the tamper (right).

5.3.2 Average Scan Reduction

The median polish method provides excellent reduction of common mode signals in both dimensions, but is relatively computationally intensive and time-consuming as the algorithm iterates to convergence. Toward the goal of faster algorithms more suitable for real-time analysis, PNNL explored other options for common-mode rejection, in the context of the expected characteristics for Mantis signals. For example, in the median polish discussion above, the synthetic Mantis data matrix had sinusoidal trends in both dimensions. In practice, however, this is unlikely to be the case for actual Mantis monitoring. Rather, it is expected that significant, common undulations are present primarily in the x (distance) dimension, due to correlation structure common to each scan. In the y (time) dimension, where drift in the Mantis transmission amplitude is expected to be the primary source of systematic change, relatively modest and approximately linear trends are anticipated, at least over the expected analysis time scales (seconds to minutes).

Based on this assertion about the likely characteristics of Mantis signals during a given analysis period, PNNL studied a relatively simplistic signal processing method that subtracts the baseline of a data set and removes the average value of each scan line. This is accomplished by using the first scan line of the data set as the baseline, which removes/reduces the sinusoidal trend in the x dimension. Next, the average value in every scan is removed, this helps eliminate system drift and any offset from the baseline scan. Scoping analyses indicated that this baseline subtraction and average reduction (BSAR) method can be completed 100-500 times faster than a full implementation of median polish.

Improved speed is an advantage, but the key technical question is whether this simplified method is sufficiently effective for IAEA use cases. To preliminarily investigate the method’s effectiveness, PNNL created another synthetic Mantis data set (Figure 13) that exhibits the following characteristics: linear amplitude drift as a function of start time, a sinusoidal trend in the distance dimension, no Gaussian noise, and a simulated tamper in the lower right quadrant.

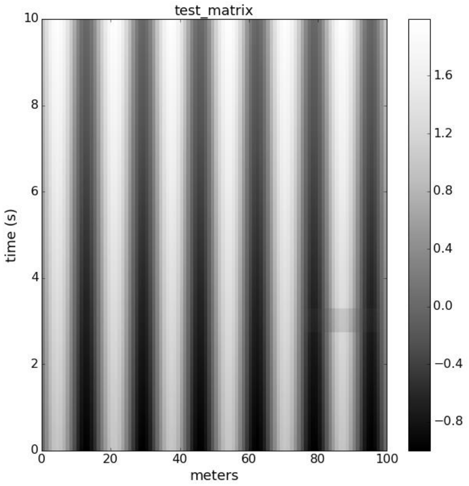

Figure 13. Simulated Mantis raw data matrix (left) with a sinusoidal trend in the distance dimension, linear trend in start-time dimension, no Gaussian noise, and a simulated tamper in lower right quadrant of the matrix.

This synthetic data set was then processed using both the median polish and BSAR algorithms. The results are shown below in Figure 14. Median polish produces impressive contrast for the tamper, as expected, but the more simplistic algorithm also significantly improves the contrast of the simulated tamper. This method also produces an abnormality in the scan lines that span the tamper this is due to the amplitude of the tamper influencing the average value in the x dimension. Upon closer inspection of the tamper event in the distance dimension (Figure 15), it is observed that there is only a shift in the amplitude still preserving the relative SNR between the artifact and the rest of the trace. In the time dimension (Figure 16), there is a slight reduction in the relative amplitude of the artifact in its specific spatial bin as compared to other points in time where the artifact is not preset. The simplistic approach shows a loss of 1.25dB SNR and will provide much fast signal processing on systems with limited computational power.

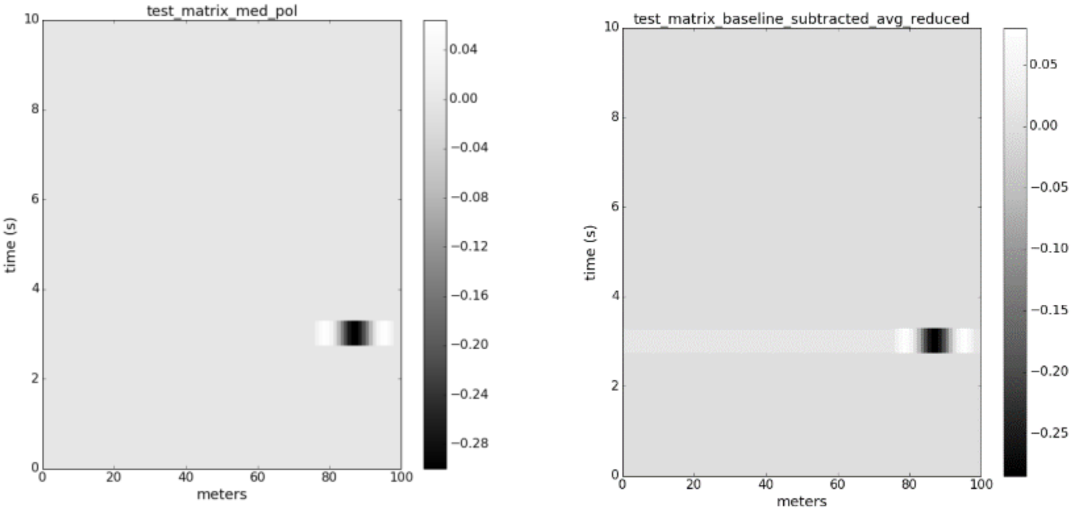

Figure 14. Post-processing version of the Figure 12 raw data, using median polish (left), and baseline subtraction and average reduction (right).

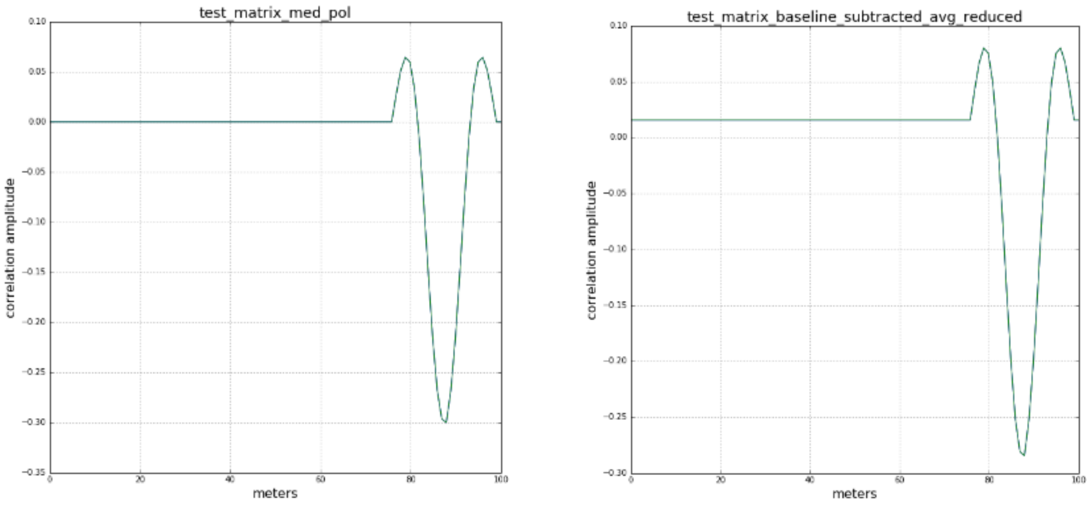

Figure 15. Individual scan profiles, during the tamper event, for raw data processed using median polish (left) and baseline subtraction and average reduction (right).

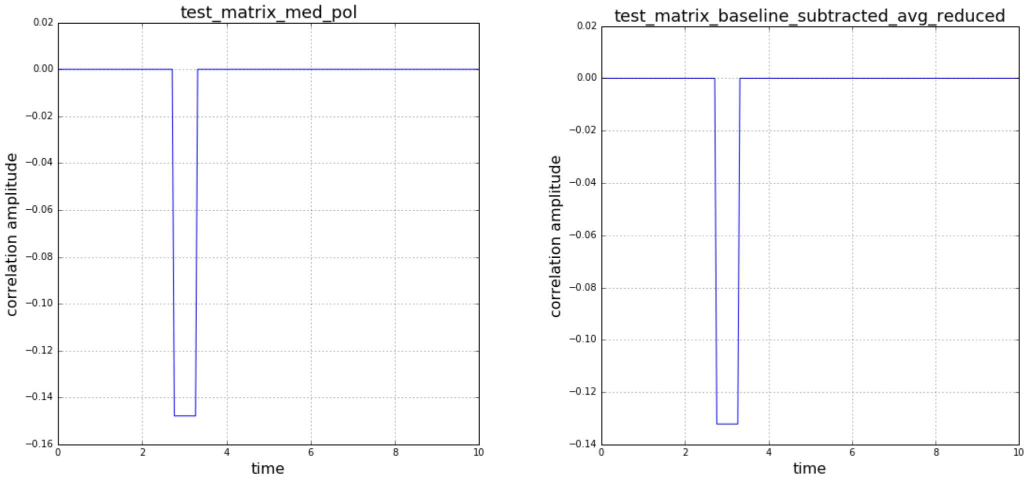

Figure 16. Data slices, at a distance of 85 meters, across all start times for raw data processed using with median polish (left) and baseline subtraction and average reduction (right).

5.3.3 Frequency Domain Filtering

The synthetic Mantis data sets used above did not include Gaussian (i.e., white or speckle) noise, but in practice, such noise will be ever-present. Therefore, TDR analysis algorithms must also be capable of removing, or at least mitigating the effects of, such system noise. In order to isolate the characteristics of the tampers from the noise inherent in the Mantis system, a digital frequency domain low pass filtering technique was employed. PNNL's implementation of the ideal digital low pass filter, referred to as Fast Fourier Transform FFT filtering, is taken from [12] and coded in Python.

The parameters for a Fast Fourier Transform (FFT) filter were defined by recognizing that, for the parameters used in this study, Mantis scans occur on the order of 800 scans / second. This means that the amplitude variation from scan to scan can change up to 800 times per second, whereas a physical tamper performed by a human being will likely be on the order of a second or more. This equates to a tamper having a rate of change for the tamper of ~1 Hz, while the noise spans sevearl hundred Hz. Thus a digital filter can be designed to pass low frequencies while rejecting high frequency content; thereby improving the contrast between the tamper signal and the system noise. Figure 17 below shows the data matrix of a Mantis data set that has been processed to remove the background signal structure and the resulting frequency spectrum in three dimensions. Note that due to finite frequency sampling, negative frequencies are also shown in the plot. This figure illustrates that at the point in space where a tamper occurs, there is a large amplitude of low frequency content, whereas where the tamper is absent, only high-frequency content from noise exists (and at relatively low amplitude).

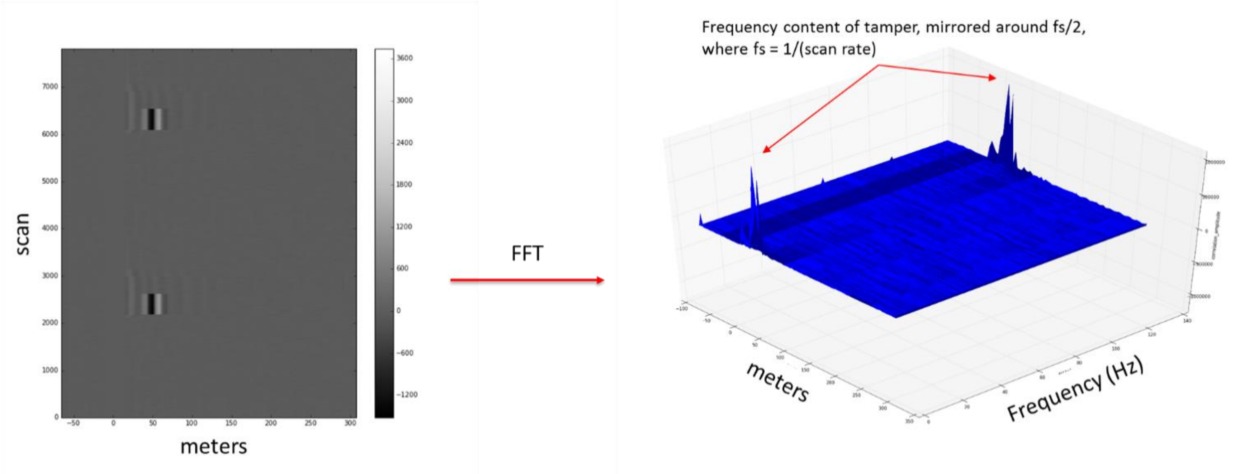

Figure 17. Left: Measured Mantis data matrix with tampers in two locations. Right: three-dimensional plot of frequency spectrum of the data matrix.

To further demonstrate the ability to utilize the FFT low pass filtering, a synthetic Mantis data set was generated with the same sinusoidal trends that were previously demonstrated in section 5.3.2, but in this data set, Gaussian noise was included along with a tamper in the lower right quadrant of the data matrix (Figure **17**8, left). Figure 18 (right) demonstrates the use of a digital low pass filter designed to reject the high frequency noise content. Note that noise has both high- and low-frequency structure so some noise will remain after the data set is low-pass filtered, albeit with an overall reduced amplitude.

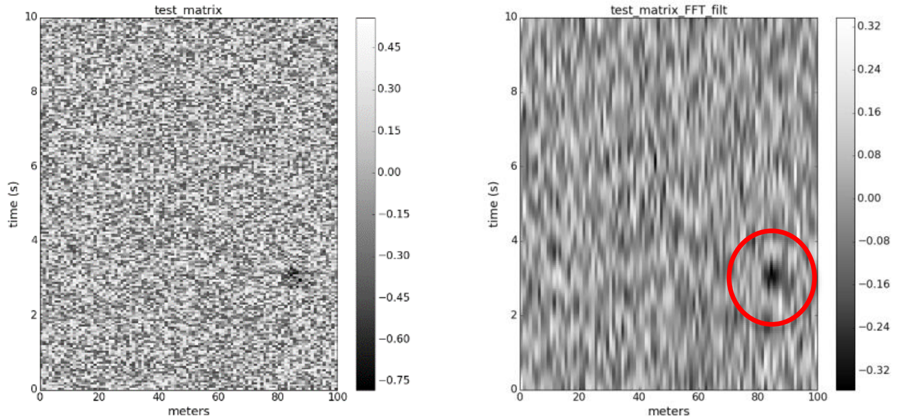

Figure 18. Simulated Mantis data matrix (left) with Gaussian noise and a simulated tamper in lower right quadrant of the matrix. Processed data, post frequency domain filtering, improves the contrast of the tamper (right). Note the different grey-scale ranges for the two cases, illustrating the noise reduction provided by FFT filtering.

5.3.4 Compilation of Signal Processing Techniques

An initial performance evaluation of signal-processing effectiveness was undertaken by analyzing synthetic data sets with and without a simulation tamper, using a combination of algorithms described above. The purpose of analyzing both data sets will demonstrate the signal to noise ratio for each signal processing set. If signal processing techniques were only performed on data sets where a tamper was being isolated, algorithms would be tuned for maximum tamper amplitude but not take into account baseline noise rejection. Likewise algorithms that focus only on minimizing the baseline noise can also negatively impact tamper amplitudes. Thus it is important to analyze both data sets and look at the relative amplitude from the tamper data set to the baseline data set as a SNR, and which techniques provide the best SNR.

These simulated data sets are shown below has and have the following characteristics: Gaussian white noise, a linear amplitude drift over time, and a sinusoidal trend in the distance axis. The first data set is a baseline with no simulated tampers, while the second data set includes a simulated tamper at 85 meters occurring at nominal scan start time of 3 seconds. In this case the tamper is barely visible in the raw data set--it is significantly masked by the drift, noise and data structure. The raw data for the baseline and with-tamper data matrices were then analyzed with different combinations of the signal processing algorithms described above: 1) FFT filtering then median polishing, and 2) FFT filtering then BSAR in both the time and distance dimensions.

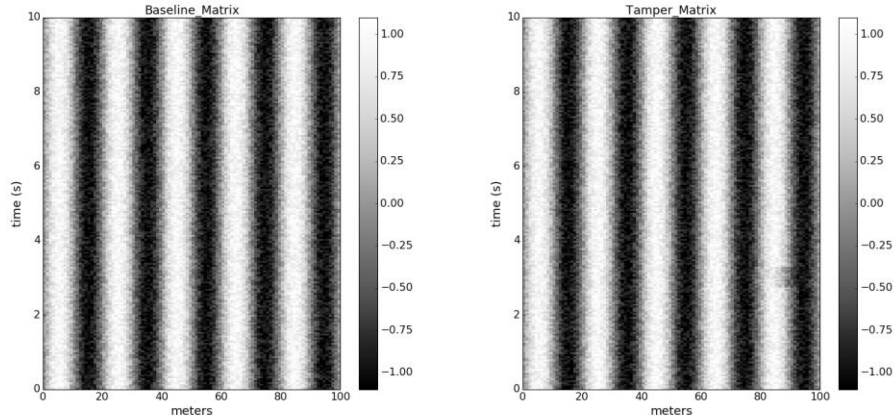

Figure 19. Synthetic Mantis raw data sets without a tamper (left), and with a tamper in lower right quadrant (right).

The baseline and with-tamper data matrices following the application of FFT and median polish are shown in Figure 20. There it is visually clear that the algorithms remove the systematic undulations in the baseline data set (left pane), essentially reducing it to a relatively low level of white noise (~10 times lower in magnitude than the original data matrix). The processed with-tamper matrix (right pane) clearly separates the tamper from the white noise (in this case, well separated from the noise in terms of correlation amplitude). Histograms of these data matrices can be calculated to indicate the signal-to-noise ratios that might be realized using the signal processing combinations. Figure 201 shows the histograms from the matrix data sets shown in Figure 19. These histograms reveal that the absolute peak noise amplitude is 0.16, while the absolute value of the tamper max amplitude is 0.27. Taking 20 * $\log_{10}(0.27/0.16)$ equates to a measured SNR of 4.55dB. Note that this SNR is not necessarily quantitatively comparable to the performance that would be achieved in real Mantis data sets, but is used to compare the effectiveness of this signal processing set to the next case.

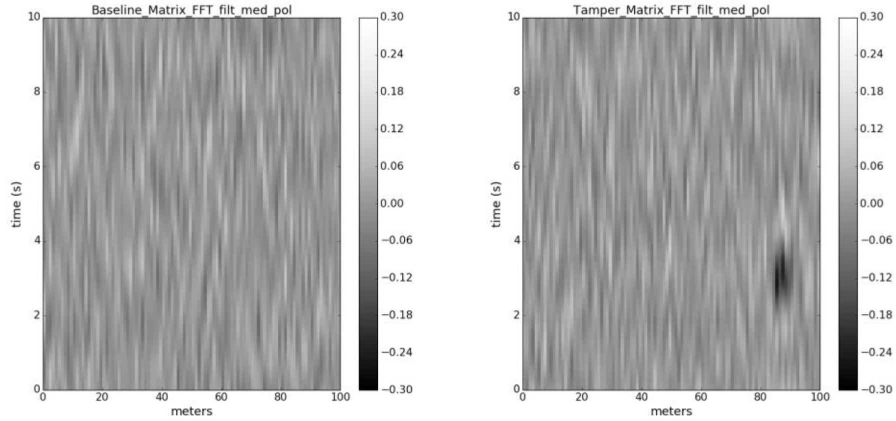

Figure 20. Example processed data matrices, using a combination of FFT filtering and median polish, for the without-tamper (left), with-tamper (right) synthetic raw data given in Figure 19.

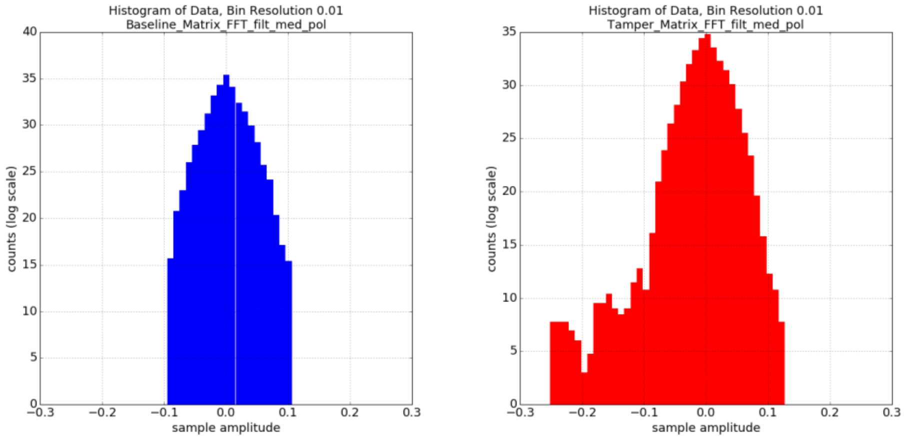

Figure 21. Histograms of complete data set values for the without-tamper (left) and with-tamper analyses, utilizing the FFT and median polish combination.

For the FFT and BSAR signal processing combination, the results are quite similar to those shown above. The FFT and BSAR combination also reduces the baseline data set to noise and improves the contrast of the tamper, as shown in Figure 22. Histograms of these data matrices (Figure 223) indicate a peak noise amplitude of 0.16 and a tamper maximum amplitude of 0.25. Taking 20 * $\log_{10}(0.25/0.16)$ equates to a measured SNR of 3.88dB.

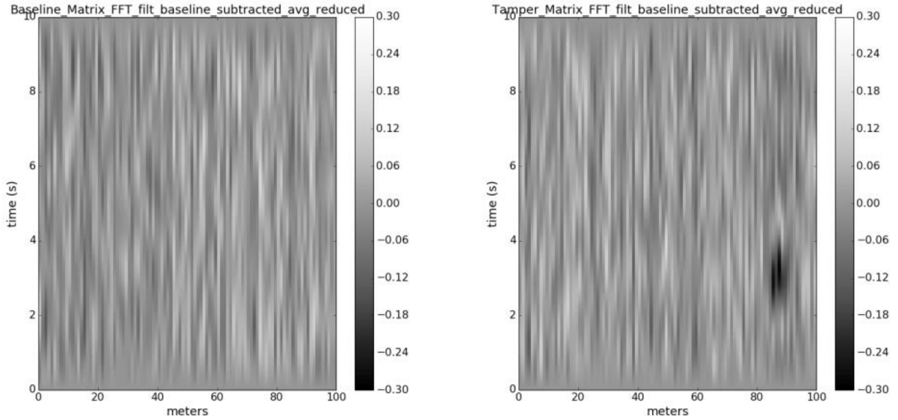

Figure 22. Example processed data matrices, using a combination of FFT filtering and BSAR, for the without-tamper (left), with-tamper (right) synthetic raw data given in Figure 19.

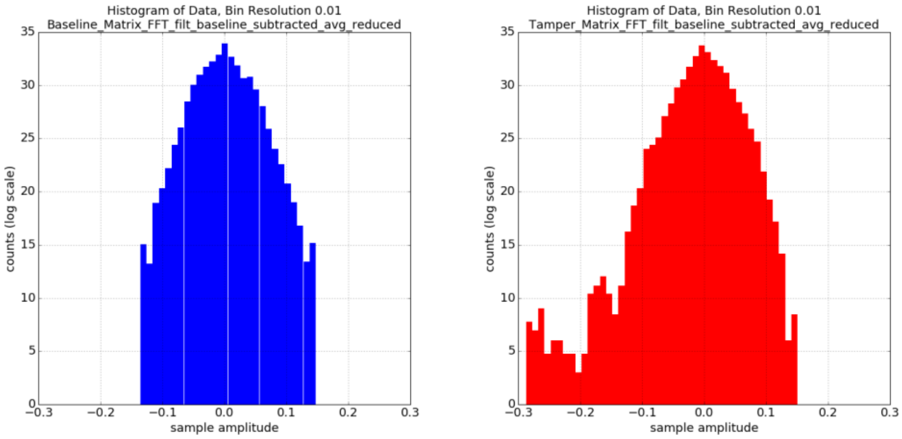

Figure 23. Histograms of the complete data set for the without-tamper (left) and with-tamper analyses, utilizing the FFT and BSAR combination.

The signal processing techniques described above were developed over the course of FY16 in order to improve detection sensitivity, reduce false alarm rates and allow near-real-time processing of the raw Mantis data. Each of the signal processing algorithms and combinations thereof has its strengths and limitations, but PNNL's preliminary finding is that the signal processing technique FFT filtering and BSAR shows particular promise for the Mantis data and an IAEA use case focused on physical tampers. Based on this interpretation, the FFT filtering and BSAR has been the standard analysis tool for the preliminary performance evaluations described below.

5.4 Event Identification and ROC Curve Analysis

Analysis for the IAEA UMS application will require algorithms that can efficiently analyze each scan for "events", and then apply alarm thresholds to flag specific events that need further investigation by the IAEA. To date, the extraction of events from a given Mantis scan has taken a relatively simple form: locating the absolute maximum value in the scan (Figure 24).

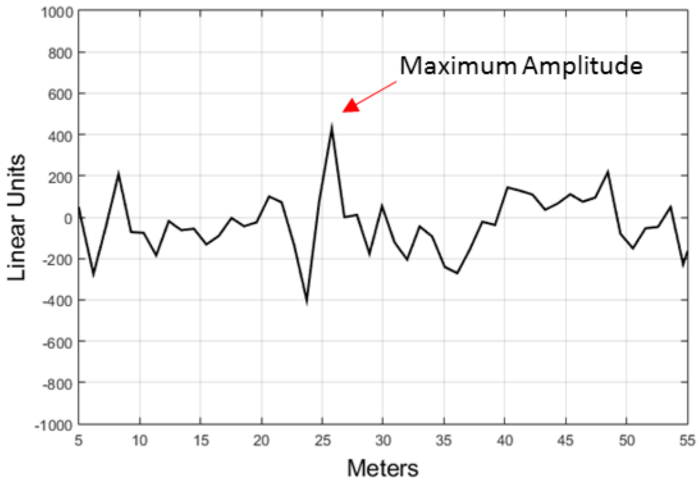

Figure 24. Example of event extraction based on the maximum amplitude in a single Mantis scan.

Once the maximum value has been determined for each scan, those values are stored in histograms that enable subsequent analysis by any number of performance metrics. All of those metrics begin with the application of a threshold. As discussed previously, the amplitude of tampers decreases with increasing cable length, but that is not generally true for the system noise. Therefore, the use of a spatially dependent (as opposed to a fixed) threshold is appropriate. PNNL has developed analysis tools for the application of both fixed (left pane, Figure 25) and spatially variable (right pane, Figure 25) thresholds in the performance evaluations. While the analysis in FY16 used fixed thresholds, it is anticipated that future work may employ spatially dependent thresholds, particularly when cables are in harsh environments in terms of RF background.

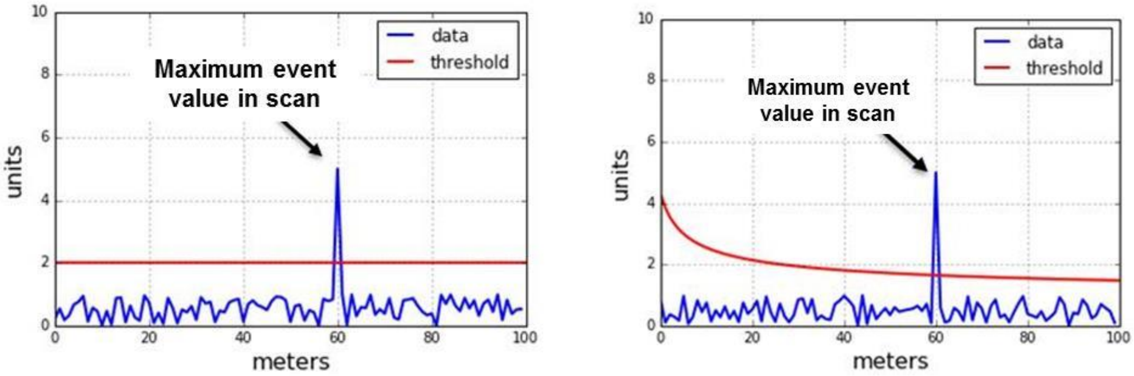

Figure 25. Depiction of fixed (left) and spatially dependent (right) thresholds as applied to the maximum event amplitude of each TDR scan.

The performance evaluations performed by PNNL in this TDR viability study should acknowledge the need for high detection probability while minimizing false alarms. The tradeoffs between the probability of detection (PD) for a given intrusion scenario and the false alarm rate (FAR) that must be tolerated to achieve that detection probability are often quantified using Receiver-Operator Characteristic (ROC) analysis; this metric has been adopted for this study.

For tamper-indication studies, ROC analyses are based on histograms of two large sample populations: 1) baseline (no-tamper) samples and, 2) with-tamper samples. FAR is mapped as a function of alarm threshold on the baseline histogram, then PD is mapped against alarm threshold on the with-tamper histogram (Figure 26 & Figure 27). The relationship between PD and FAR can then be depicted in a ROC curve (Figure 28).

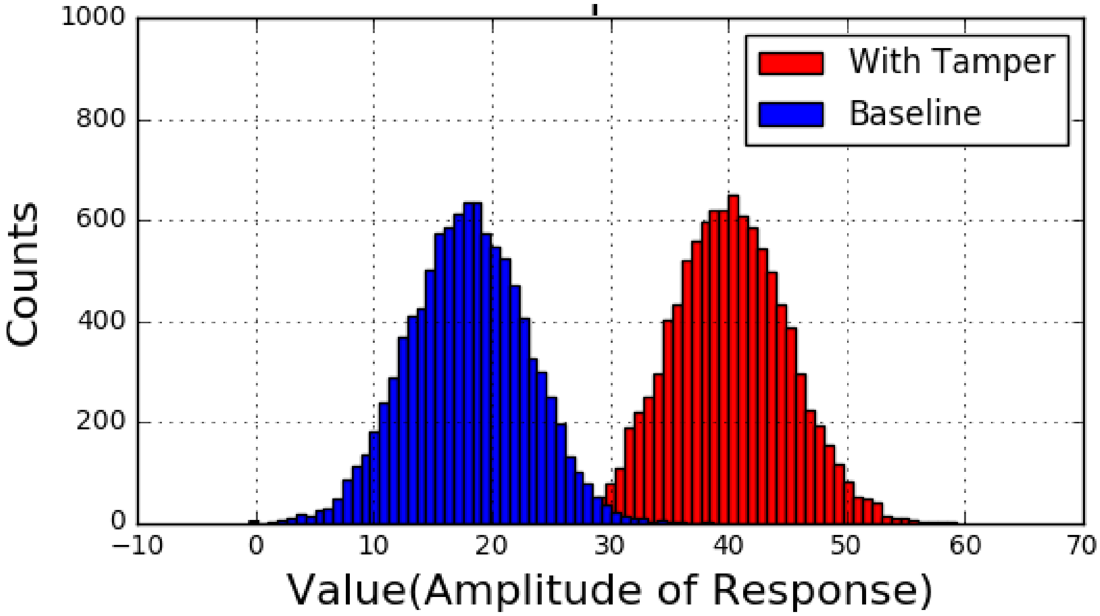

Figure 26. Example histograms, based on simulated data, of baseline (blue) and with-tamper (red) scan histograms.

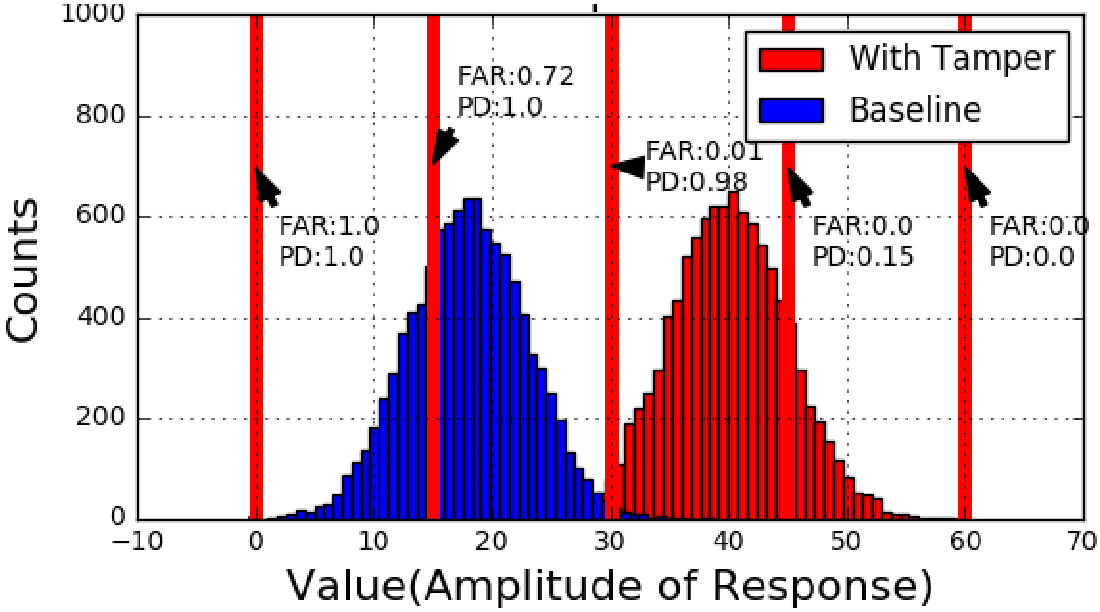

Figure 27. Illustration of how varying alarm threshold is used to map FAR versus PD for the baseline and with-tamper distributions, respectively.

Application of single threshold value to both the baseline and with-tamper histograms provides one point on the ROC curve. To build up the complete ROC curve, multiple thresholds are applied, ranging from 0 to above the highest value of either histogram as shown in Figure 28.

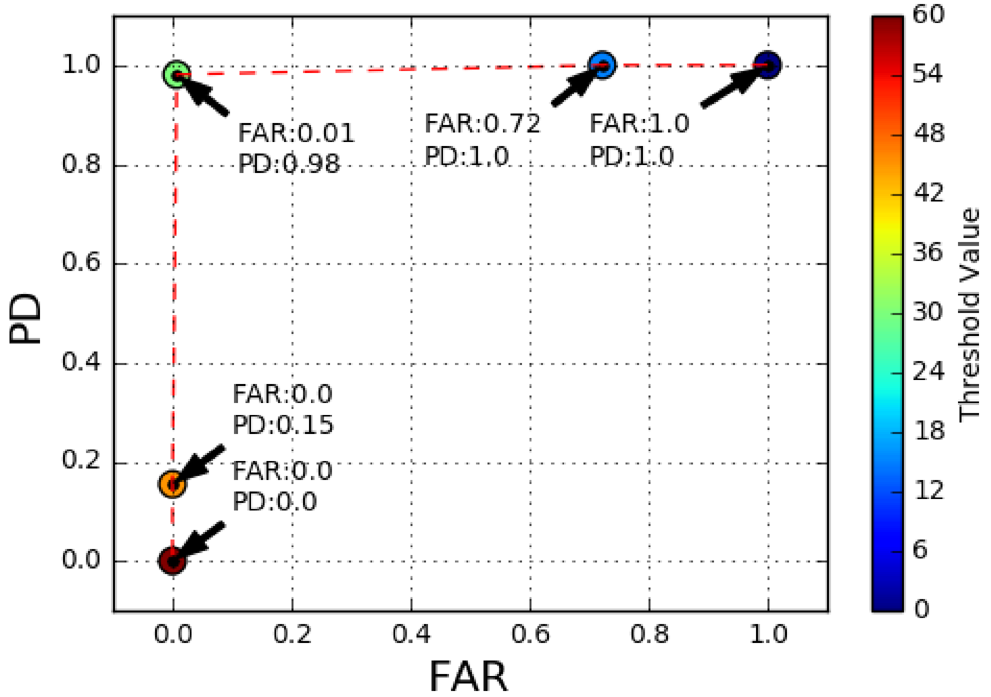

Figure 28. Example ROC curve derived from the illustrative data in Figure 26 and Figure 27.

6.0 Measurement Studies and Prototype Adaptations

The sections that follow describe a series of measurement studies that address specific technical questions, including those described in the Introduction. Generally speaking, the testing progresses from idealized to more realistic implementation scenarios and through that progression, the need for and results from, various prototype adaptations are described.

6.1 Comparative Performance Evaluation: Scoping Study

When PNNL adopted the Mantis platform in early FY16, it was necessary to determine if the Mantis system has similar performance to the ASIC-based device studied previously by PNNL for IAEA applications. This continuity check was accomplished by performing a comparison of detected signal responses from the ASIC, Mantis and VNA for various impedances at the end of a cable. The measurement systems under test are shown below in Figure 29. The low frequency VNA operated in a frequency range of 5Hz – 100MHz for these measurements. As discussed previously, the VNA performs a swept frequency measurement collecting amplitude and phase vs. frequency and then performs an inverse Fourier transform in order to convert the wide bandwidth of data into the time domain, producing an amplitude vs. time (or distance) similar to what the ASIC and Mantis systems produce.

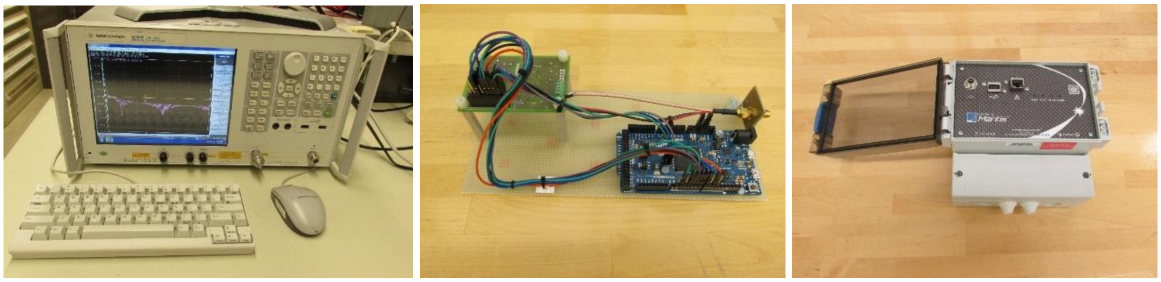

Figure 29. Measurement systems: VNA (left), LiveWire ASIC (middle), and LiveWire Mantis (right).

Both the ASIC and Mantis system perform SSTDR measurements, but the ASIC digitizes the received signal and performs correlations in the digital domain, whereas the Mantis system performs its correlation in the analog domain. The digital SSTDR technique allows for very fast measurements, but tends to have a more noisy response than the analog technique.

There is an inherent difference in the way the SSTDR systems and the VNA FDR systems display their data. The VNA measures both the amplitude and phase and thus produces a complex signal magnitude composed of both the real and imaginary signal components. The SSTDR systems produce a real-only correlation response with a linear amplitude and therefore it is not simple to compare performance from system to system. In order to accurately compare the relative SNR across the three TDR systems, for different impedance changes, the imaginary component of the SSTDR data was computed using the Hilbert transform [13]. The Hilbert transform is a well-known technique for calculating the imaginary component to a real – only data set by converting the data into the frequency domain, filtering out the image (or negative frequencies) and converting back into the time domain will produce a complex signal.

Once the imaginary component of the SSTDR data was calculated, the complex magnitude in terms of dB was calculated and compared to the VNA result.

The measurement parameters for each of the TDR systems is shown below in Table 1. Note that the VNA is configured to have very high performance for this measurement, focusing on measurement sensitivity rather than speed. The ASIC system is designed differently than the Mantis system and therefore the integration times are not a direct comparison. The amplitude levels used for the ASIC and Mantis systems were amplitudes that had been shown in previous studies with the ASIC to not interfere with detected energy spectra.

Table 1. Measurement system settings.

	VNA	**LiveWire ASIC**	**LiveWire MANTIS**
Sample pts	210	91	76
Averages	None	200	200
Voltage	632mVpp	128mVpp	132mVpp
Frequency range	5Hz-100MHz	24MHz	24MHz
Integration time	NA	512us	160us

The measurement systems were tested against a 50-meter long RG-174 (50 Ohm) coaxial cable. Different loads were placed at the end of the cable (Figure **29**30) in order to compare the performance sensitivity of each system.

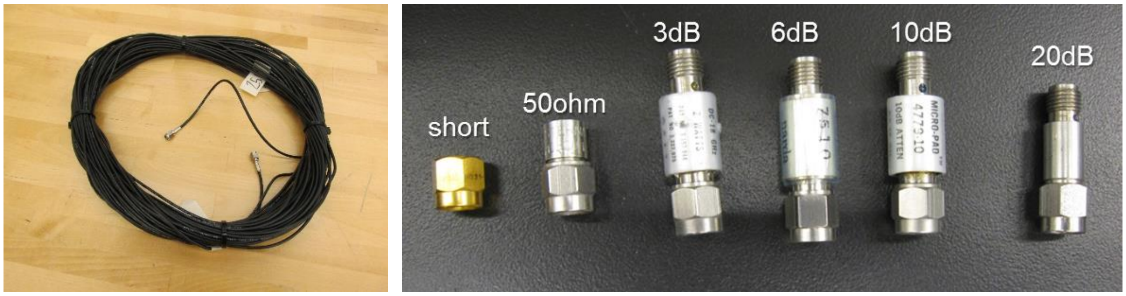

Figure 30. Test cable and devices for comparative scoping study of VNA, LiveWire ASIC and LiveWire Mantis.

Example results from the impedance tests are shown below for all three systems, for a short circuit at the end of the cable. In this case the VNA is demonstrating nearly an order of magnitude better SNR, and the ASIC and Mantis system are nominally the same.

Figure 31. Magnitude of reflection for short circuit at end of cable for VNA (left), LiveWire ASIC (middle), and Mantis (Right).

A summary of the results from the comparative scoping study is shown below in Figure 32. As expected, the VNA stands out as having higher sensitivity than both the SSTDR systems since the VNA is tuned to have optimal detection in terms of bandwidth, power, and sampling. The VNA can be viewed as a baseline for the best-achievable SNR for active TDR systems, a standard to which the lower-cost instruments can be compared. Note that while the VNA is a laboratory gold standard system with very high performance, but may be impractical for the IAEA UMS application due to system cost. The cost of the VNA system used in this study is nominally US $40K while the integrated Mantis system is approximately US $5K, and the Mantis board stack—a potential form factor for the UMS prototype, is US $3K.

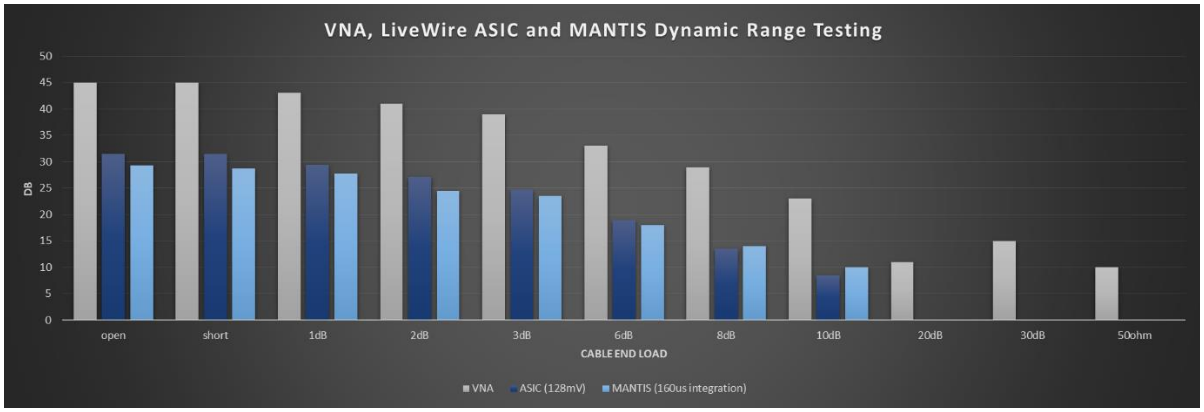

Figure 32. Comparative scoping study results for VNA and two LiveWire SSTDR variants.

As shown in Figure 31, the performance of the ASIC and Mantis were essentially identical for the range of tests performed in the scoping study. With this check on the continuity of functions and performance completed, PNNL moved forward with Mantis as the form factor of interest for the viability investigation of LiveWire's SSTDR method.

6.2 Mantis Performance: Baseline without Radiation Sensor Signals

Figure **7**8 and Figure **8**9 describe the nominal equipment configuration, and tamper methodology, for Mantis testing and performance evaluation. To set a baseline on Mantis performance for monitoring UMS cabling, a tamper-detection study was performed in which the UMS detector (i.e., NaI(Tl) spectrometer) was in place and powered, but recorded only the nominal background in the laboratory. That is, no radiation source other than ambient background is in place and therefore, the count rate in the detector is relatively low, approximately 100 cps. For these measurements, the 3 Port Interface is an unmatched SMA Tee, used for simplicity of connections. The instrument rack was populated with the TDR test equipment, Pocket MCA, VNA, power supplies and host computer, similar in function and components to the cabinets deployed by the IAEA UMS.

As depicted in Figure **8**9, the 50-m RG-174 cable had small cuts made into its outer conductor at 0, 1, 5, 10, 15, 20, 25, 30, 35, 40, 45, 49, and 50m to represent the physical tampering associated with the taps using the oscilloscope probe.

The set of measurements collected in the baseline performance study are described in Table 2. For each tamper location, a 10-minute data set was collected that consisted of approximately 100,000 TDR scans of the cable at each tamper location. 50 physical tampers were also performed during the 10-minute data acquisition period. The duration of each physical tamper was approximately four seconds; the frequency was approximately one tamper every 12 seconds.

Table 2. Summary of measurements for baseline performance study.

#	Measurement Name	Tamper	# of Tampers	Tamper Duration	Scan Duration
1	TDR baseline	off	0	NA	10mins
2	0m_Tamper	on	50	4 sec	10mins
3	1m_Tamper	on	50	4 sec	10mins
4	5m_Tamper	on	50	4 sec	10mins
5	10m_Tamper	on	50	4 sec	10mins
6	15m_Tamper	on	50	4 sec	10mins
7	20m_Tamper	on	50	4 sec	10mins
8	25m_Tamper	on	50	4 sec	10mins
9	30m_Tamper	on	50	4 sec	10mins
10	35m_Tamper	on	50	4 sec	10mins
11	40m_Tamper	on	50	4 sec	10mins
12	45m_Tamper	on	50	4 sec	10mins
13	49m_Tamper	on	50	4 sec	10mins
14	50m_Tamper	on	50	4 sec	10mins

One of Mantis's standard signal processing techniques is refreshing the system baseline every ~30sec to remove any system amplitude drifts. This approach was adopted by limiting the duration of the data that was processed to be less than this time window. Therefore, each 10-minutes data set was split into fifty 12-second segments. For each segment, the data was processed using the same signal processing methods and parameters. The baseline data set was also segmented and processed in the same way, in order to produce an accurate measurement of the system noise, which could then be compared to the tamper amplitudes. An example of a processed Mantis data matrix is shown in Figure 33. The raw data was analyzed using the FFT and BSAR signal processing method, thereby improving the contrast for detection of the physical tamper at 25m, 4 seconds in duration.

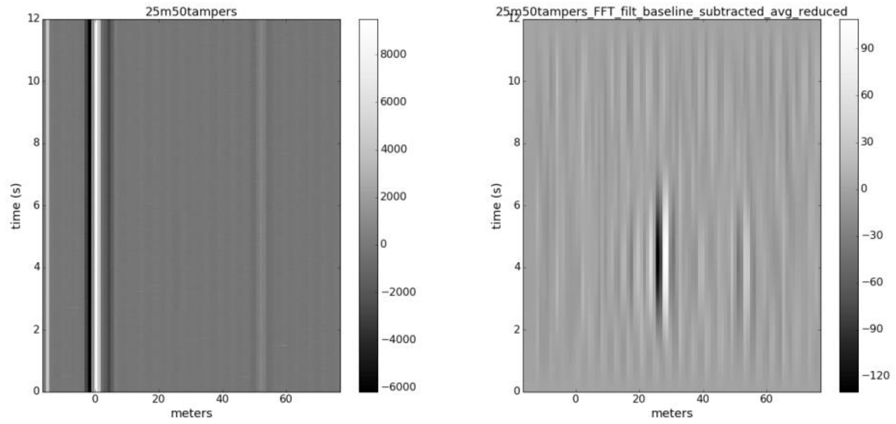

Figure 33. Measured Mantis raw data matrix (left) for a physical tamper at 25m between 2 and 6 seconds in scan start time. Processed data, post FFT and BSAR, significantly improves the contrast for tamper detection (right).

A more quantitative presentation of the contrast between tamper events and system noise is given in Figure 34, where the amplitude of each manual tamper event (green dots) is compared to the maximum amplitudes from each scan in the baseline (no tamper) population. Observations on Figure 34 include:

- The amplitude of tamper events decreases with increasing cable length, as expected (and discussed previously in this report), and motivates the exploration of spatially dependent thresholds.
- Generally speaking, the tampers are well separated from the baseline system noise, after application of PNNL’s signal processing algorithms, but there are some low-intensity tampers for which this is not the case.
- There is high variability in the amplitude of tamper events, particularly on the low-intensity side. These tampers are likely due to human error/variation in the installation of the physical tamper such that the tamper was not completely installed. Greater consistency and larger tamper sample sets are some of the motivation for PNNL’s development of an automated tamper apparatus (see Section 7.2).

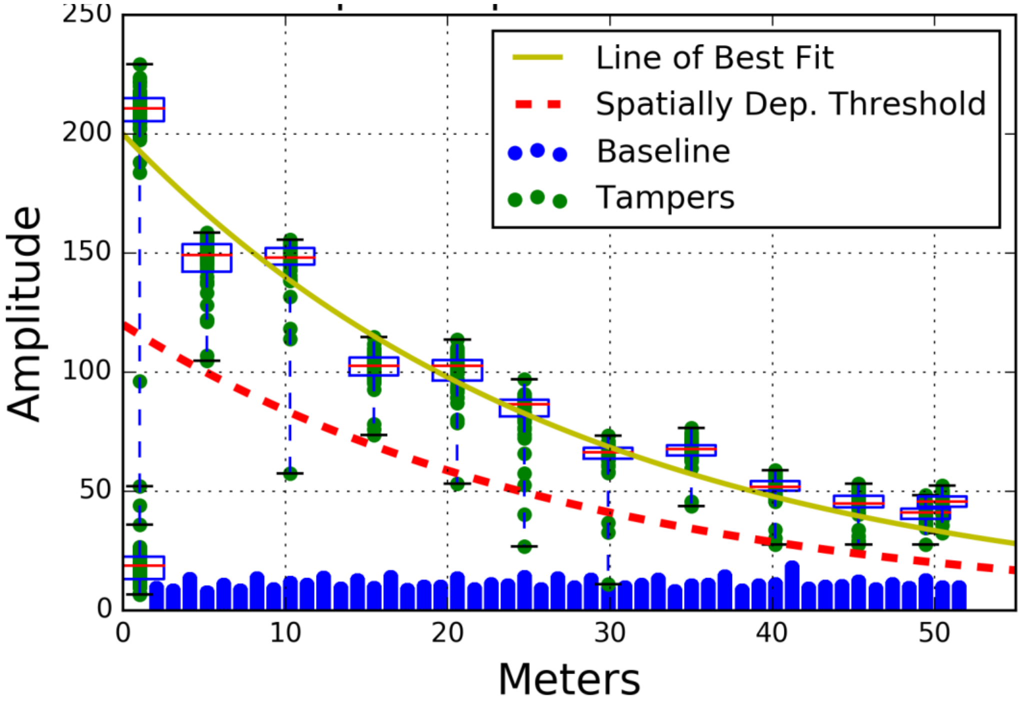

Figure 34. Summary plot of tamper and baseline amplitudes vs. distance.

ROC curves were developed for the data in Figure 34 above by using a flat threshold versus distance (i.e., spatially dependent thresholds were not used) to determine the true positive (TP) and false positive (FP) events in each scan. FPs are created when noise from any scan exceeds the threshold. TPs are tallied when any portion of a tamper response exceeds the threshold. Note that only a single alarm event is tallied even though multiple scan samples stay above threshold during a tamper event. Generally speaking, the noise-generated FPs derive from a single sample in a scan, so this delineation is less of an issue.

A subset of the ROC curves produced for the baseline performance studies are shown in the following figures. The complete set of ROC curves is shown in Appendix A. As indicated in Figure 34 above, the detection of tampers at the output of the 3-port network (x=0m) is challenging due to a relatively high proportion of tampers with very low signal amplitudes—just above or in the noise. There is the potential that the physical movement of the 3 – port network during the introduction of the tamper influenced the data—more investigation is needed. Note that questionable performance at this location is not a practical problem since the 3-port network will always be located within the IAEA cabinet.

At distances beyond the 3-port network (and boundary of the tamper-indicating cabinet) the ROC performance is relatively strong and consistent. The ROC curves for 25m and 50m are perfect due to the full separation between all tamper signals and the system noise levels. This is not the case for the 30-m data, where one of the tampers lands in the population of baseline noise, thereby creating a “kink” in the ROC curve at low FAR. It should be noted that this very encouraging performance is based on a relatively small number of tampers (50), short time periods where instrument drift and anomalies are less likely to arise, and without the potential interference of high count rates from the UMS sensors.

To aid deeper interpretation of the ROC curves and thresholds used to produce them, a color bar is shown on the right that depicts the threshold level required to detect the tampers. Because some of the manual tamper signals at 0m case are quite low in amplitude, a very low threshold level is required, encroaching into the noise level. At 25m the tamper amplitudes are higher and cleanly separated as depicted by the color bar scale, showing a threshold of ~50 required to detect all the tampers at 25m.

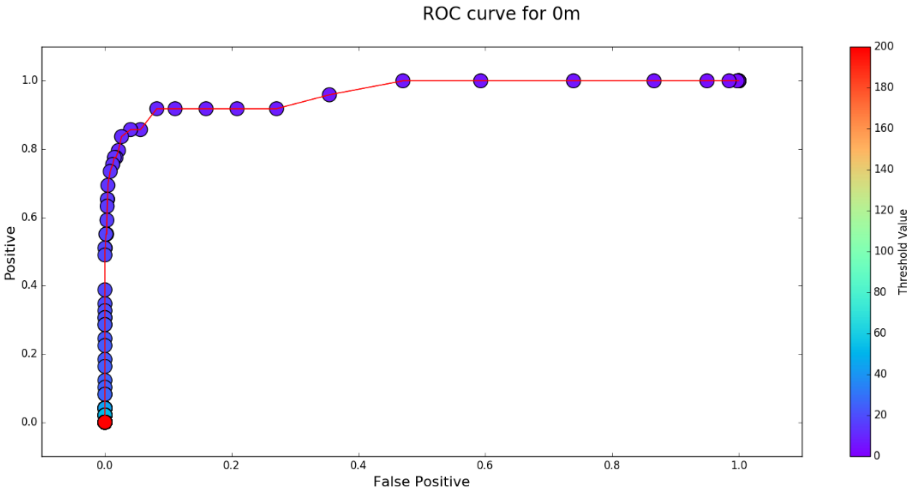

Figure 35. ROC curve for tampers at 0m.

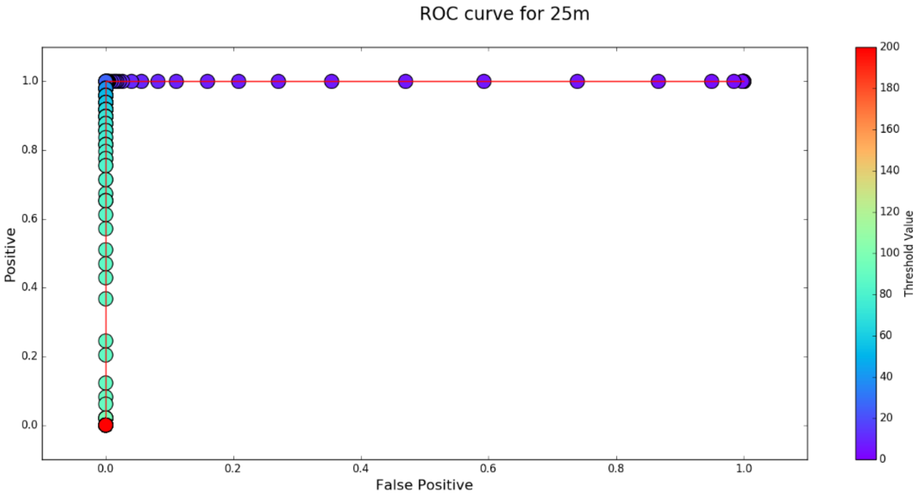

Figure 36. ROC curve for tamper at 25m.

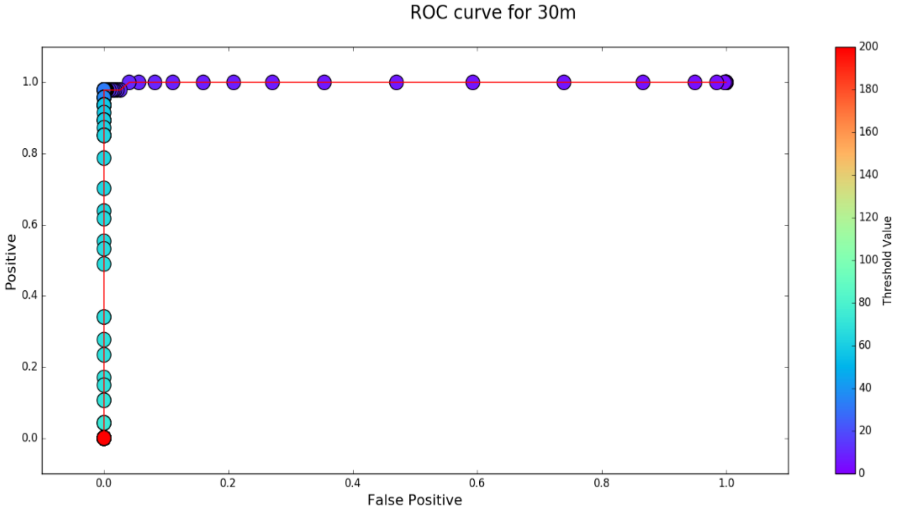

Figure 37. ROC curve for tamper at 30m

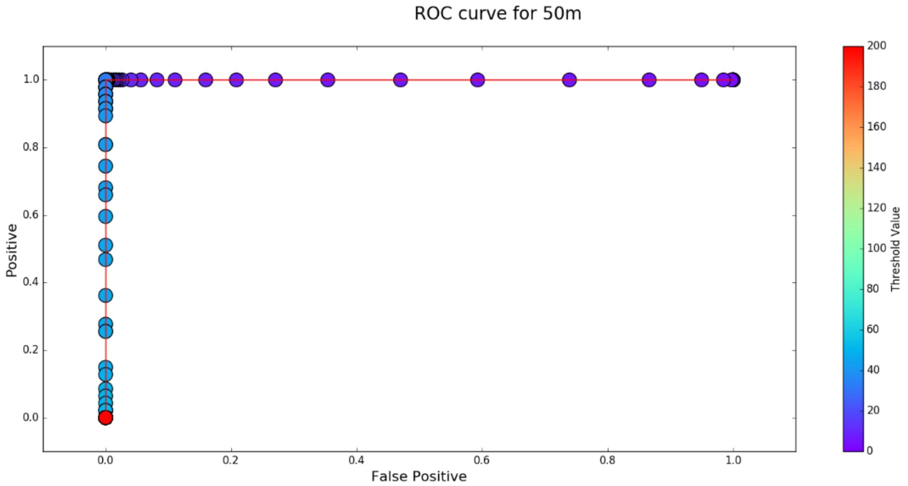

Figure 38. ROC curve for tamper at 50m

The results presented in this section for the baseline Mantis performance coupled to PNNL's post processing algorithms are encouraging, but they do not address the potential impact of interference between the UMS sensors and Mantis, because the NaI spectrometer count rate was so low (i.e., ambient background only, approximately 100 cps). The next phase of measurements was used to evaluate if higher count rates, more typical of UMS installations, impact Mantis performance and vice versa.

6.3 Interference between Mantis and Radiation Sensors

To provide an initial assessment of potential interference between Mantis and UMS radiation sensors, measurements similar to those described in the previous section were repeated, but this time with the ^{137}Cs source on the face of the NaI sensor in order to produce count rates more typical of those encountered in UMS installations. Two specific questions were of interest: 1) Do representative sensor count rates from the UMS sensor degrade the performance of the Mantis system, and 2) Do the Mantis SSTDR signals negatively impact the pulses coming from the radiation sensors?

Anecdotally, it was observed in initial measurements with the Mantis SSTDR system that detector pulses coming from the FEUM pre-amplifier and shaping circuit were detected in the Mantis SSTDR system. These radiation sensor pulses are very high in amplitude relative to the Mantis SSTDR signal changes observed for physical tampers, and thus are likely to produce false alarms if signal processing algorithms are based solely on amplitude. A quantitative study was needed, however, of how well PNNL's digital signal process techniques described earlier can separate the two signals. Figure 39 shows the histogram plots for the FFT and BSAR processed Mantis data, with and without the gamma-ray source in place. Clear from those figures is that even with digital signal processing techniques, the higher count rate from the NaI sensor produces interference and frequency structure that cannot be fully filtered using this digital combination of FFT and BSAR. The with-source histogram on the right shows nominally an order of magnitude increase in the maximum amplitude (~75 versus ~7) of the distribution, on both the high and low sides of the mean. The baseline performance studies indicated that tamper signal amplitudes, especially at longer cable distances, often have values less than 100, and thus would be undetectable with the interference presented by the higher count rates in this test. Note that the legend of 0.25Hz fc corresponds to a 0.25Hz cutoff frequency for the digital low pass filter.

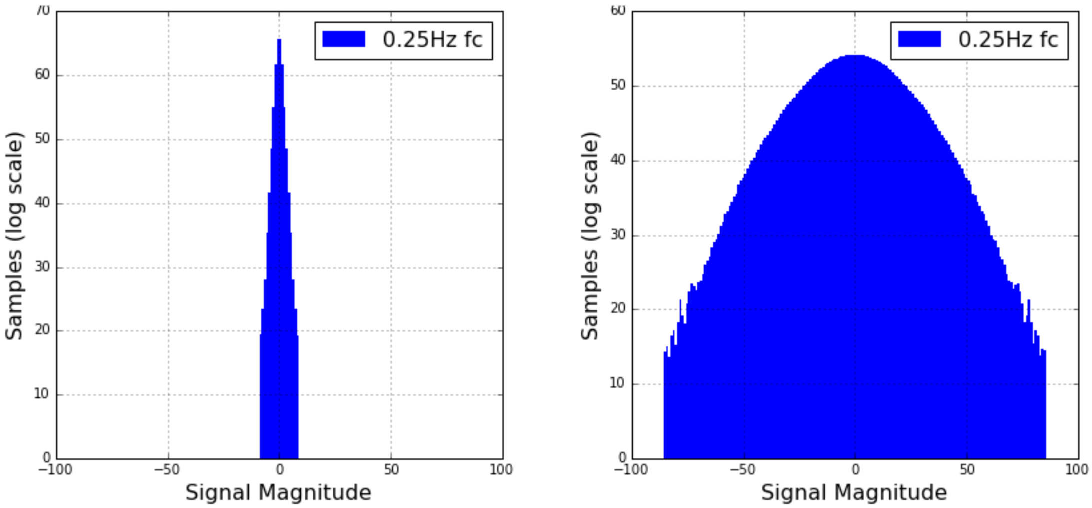

Figure 39. Comparison of Mantis noise levels, after digital signal processing has been applied: without ^{137}Cs (left) and with ^{137}Cs (right).

These results indicated that digital signal processing alone is unlikely to mitigate the interference between Mantis and radiation sensors and therefore, external filtering via hardware needs to be considered. PNNL's development of hardware filter, as an adaptation to the COTS Mantis, is discussed next.

6.3.1 High Pass Filter Development

In order to reduce the interference induced on Mantis signals by UMS, a front-end hardware filter was designed to reject the lower frequency content associated with the pulses from UMS sensors. Generally speaking, UMS-sensor count rates will range from kcps to Mcps, and each individual pulse has durations between a few hundred nanoseconds and several microseconds. This indicates that the frequency content of the UMS sensor signals is in the Kilohertz (KHz) and Megahertz (MHz) range. The Mantis TDR signal, on the other hand, contains frequency content in the KHz up to hundreds of MHz. Therefore, a filter is needed at the Mantis input that can reject frequency content in the low MHz range but pass the Mantis TDR signal high frequency content. This filter topology is termed a high-pass filter (HPF).

PNNL designed a prototype HPF in a software tool termed Ansoft Designer, and its modeled performance and component values were adopted to use as a proof of concept HPF. Figure 40 below depicts the schematic for the HPF and Figure 41 shows the fabricated HPF on a 50-ohm transmission line on a custom circuit board.

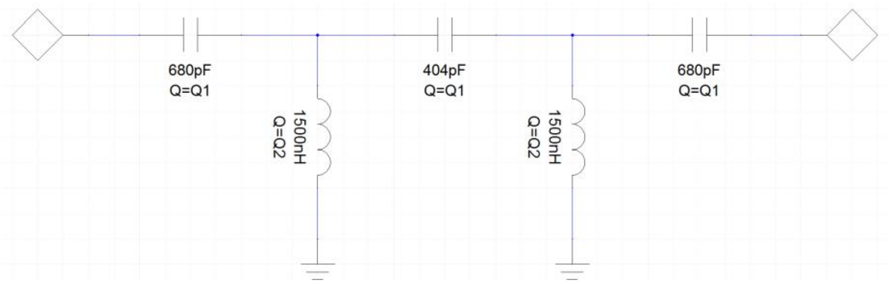

Figure 40. High pass filter circuit schematic.

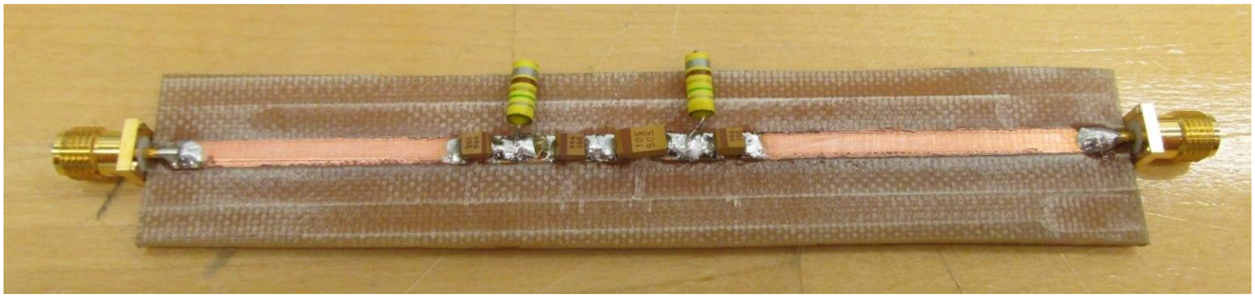

Figure 41. Prototype high-pass filter.

The performance of the HPF was measured using a low-frequency network analyzer taking a measurement from 5Hz – 150MHz. S11 shows the energy transfer into the device. A low S11 is desired in the pass bandwidth but an S11 close to 0dB is desired in the rejection bandwidth (0dB = 100% energy is reflected, -3dB = 50%, -10dB = 10%). S21 measures the transfer function through the filter, in the rejection band S21 as low as possible is desired, but in the pass bandwidth an S21 close to 0 dB equating to no energy loss is preferred. Figure 42 shows the measured performance of the HPF, with the half power (-3dB) cut off point at nominally 5MHz.

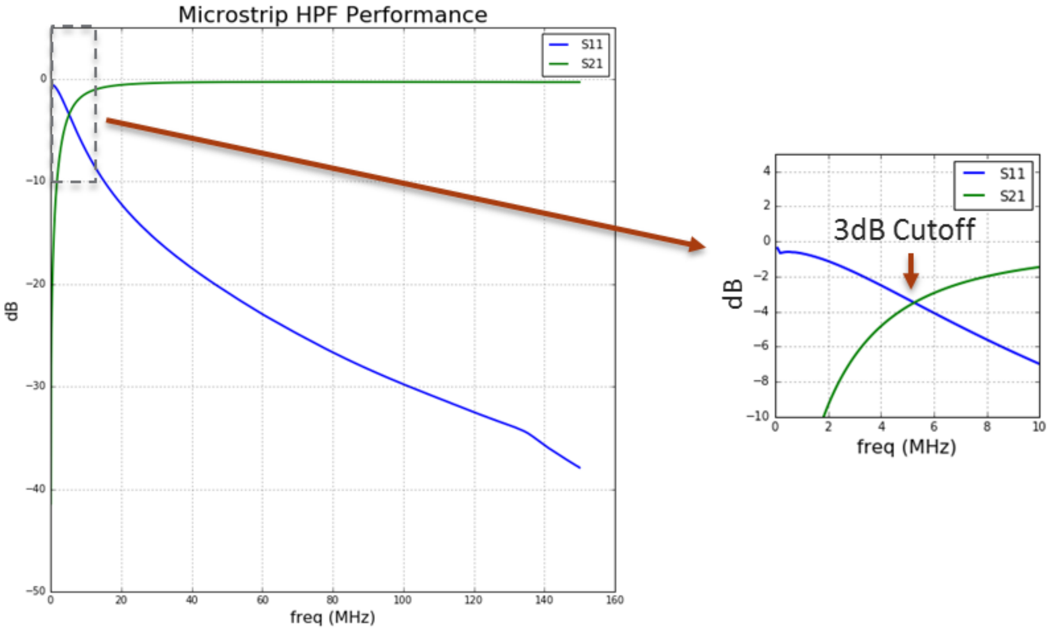

Figure 42. Measured performance for high pass filter.

As stated earlier, higher count rates from the NaI spectrometer created low-frequency noise on the Mantis signal. Figure 43 shows this interference in the measured Mantis data matrices for a case without the ^{137}Cs source (left), and with the ^{137}Cs source (right).

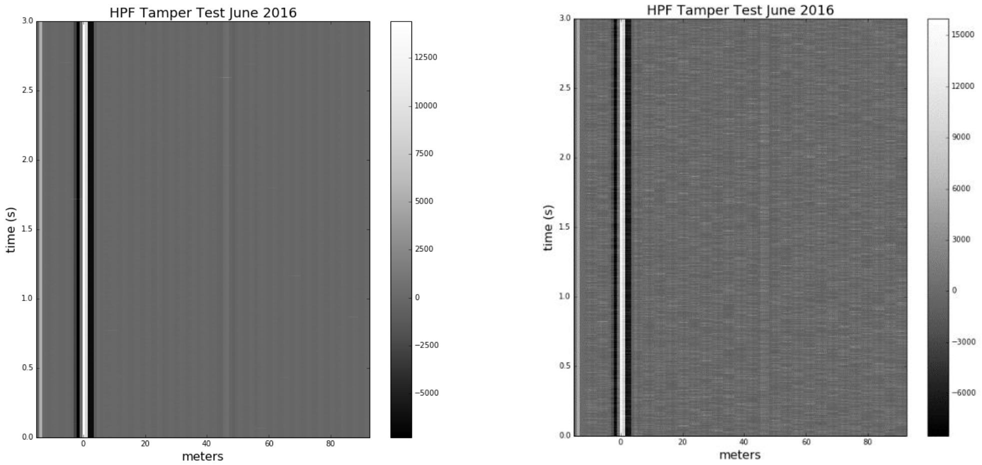

Figure 43. Unprocessed Mantis data without ^{137}Cs (left), and with ^{137}Cs (right).

Figure 44 shows the signal magnitude histogram of the complete Mantis data sets post FFT and BSAR, for measurements performed without and with the prototype HPF in place at the Mantis input. The histogram from the with-HPF case (right pane) demonstrates the ability of the HPF to reject the interference coming from the FEUM pulses. The tightening of the baseline signal responses, as accomplished with the HPF, is critical for detecting the small signal tampers that have amplitudes that would be otherwise masked by the interference caused by the pulses from the NaI sensor.

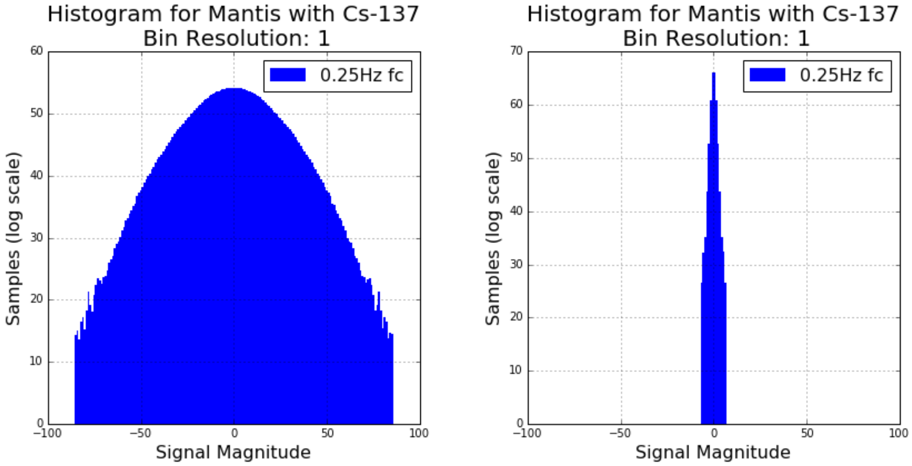

Figure 44. Comparison of Mantis noise levels when the ^{137}Cs source is present: without HPF (left), and with HPF (right).

The results above indicate that a properly designed HPF installed at the Mantis input can significantly improve the isolation between the NaI sensor signals the Mantis system, rejecting the interfering features of the sensor pulses. Another key consideration, however, is how the HPF influences the detection capabilities of the Mantis system. Mantis utilizes an SSTDR technique which spreads the energy of the probing waveform over a wide frequency range. This means that a portion of the Mantis output spectrum will be present over the frequency range where the HPF is heavily attenuating the signal. The following questions were then pursued: What effect does low frequency rejection of the Mantis spectrum have on the SSTDR signal? Does the removal of the low frequency content have any negative effects on the Mantis SNR?

A model of the Mantis SSTDR signal was made using Python scientific computing platform. The SSTDR signal was created by phase-shifting a digital pulse at the frequency utilized in the Mantis measurements, generating a binary phase shift keyed (BPSK) sequence. The digital, randomly phase-shifted pulse train was then converted into the frequency domain and passed through a digital filter that rejected low frequency content. The remaining frequency content was then brought back into the time domain using an inverse Fourier transform. And the result of the original time domain series vs. the high pass filtered series is shown below in Figure 45.

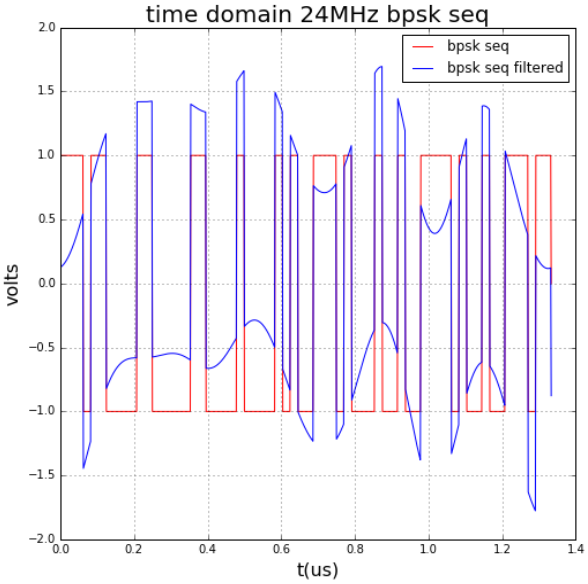

Figure 45. Result of high-pass filtering of a simulated SSTDR BPSK sequence.

It is clear that the removal of the low-frequency content causes a significant change in the BPSK sequence. Notice that the edges of the BPSK sequence that has been filtered are still sharp because high-frequency content creates the sharp edges on time domain waveforms, but the features associated with lower frequencies, for example the shape of the signal at the top and bottom of the undulations, is decidedly different.

This change is expected to reduce the correlation amplitude between the reference (shown in red) and the BPSK sequence that has been filtered, because now there is no perfect sequence overlap. Figure 46 below shows an example of the correlation amplitude between the perfect BPSK reference sequence and a perfect return sequence (i.e., correlation of the red BPSK sequences in the previous figure), and the correlation amplitude between that same perfect reference sequence and the filtered sequence that would be returned through the HPF. The results show the expected--that the filtering of the BPSK waveform reduces the correlation amplitude. As the cutoff frequency of the filter gets higher, the more low-frequency content is removed by the filter, thereby reducing the correlation amplitude even more. This simulation demonstrated the negative effect that the removal of low frequency content from the BPSK sequence, via a hardware HPF, will have on the correlation amplitude.

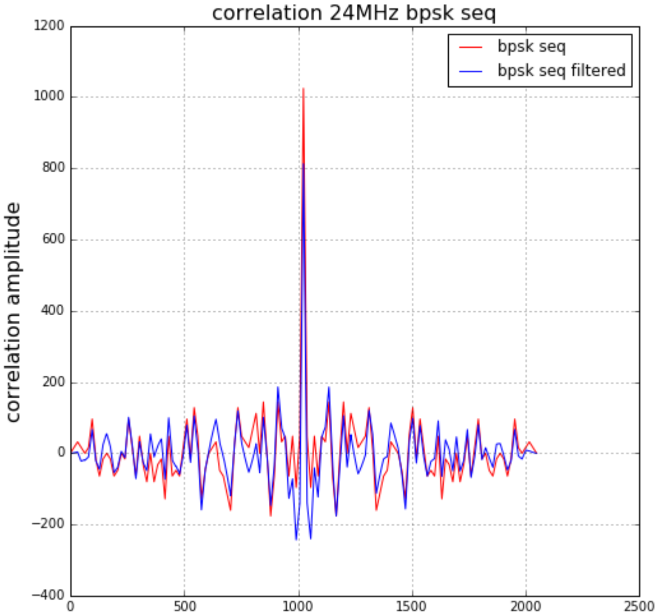

Figure 46. Correlation result for ideal signal to reference (red), and filtered signal to reference (blue).

The question as to whether the reduction in the correlation amplitude created by the HPF would have any significant impact on overall performance was then investigated. If the detection limitation on the Mantis system is due to signal strength versus thermal noise, the thermal noise will be absolute and a reduction on correlation amplitude will reduce SNR. However if the detection limitation on the Mantis system is due to correlation noise, correlation misalignments between the reference and reflected BPSK sequence, then the noise is expected to scale with the correlation amplitude. In that case, there should be little/no impact of the HPF on the SNR.

The SNR performance of the Mantis system with a HPF was tested in the measurement configuration shown below in Figure 47. Mantis's SNR for a baseline vs. its associated tamper scenario was determined for two cases, 1) HPF installed on Mantis input/output and 2) Microstrip transmission line installed, effectively a lossless transmission line, on Mantis input/output. These measurements were taken without the ^{137}Cs source, to focus the investigation purely on the best achievable SNR with and without the HPF in place.

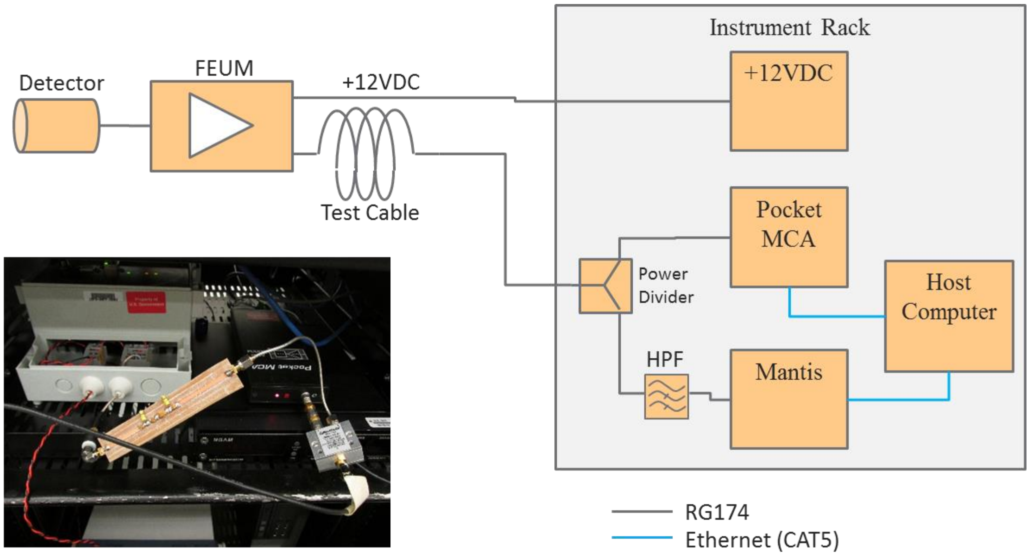

Figure 47. HPF Test Configuration

Baseline measurements for each case were collected for 10 minutes, and tampers were performed at 1, 25, and 49 meters from the Mantis system. The maximum event values for each scan were used to determine the baseline (noise) and tamper (signal) amplitudes with and without the HPF. Both the baseline and tamper data was processed using a median polish (it was not yet determined that median polish processing could be accomplished with faster algorithms such as BSAR) and FFT with a low-pass digital filter at 0.25Hz. SNR was calculated by the following equation,

$$\mathrm{SNR}=20\log_{10}(\mathrm{tamper\_max\_amplitude} / \mathrm{baseline\_max\_amplitude}).$$

The table below summarizes the SNR change in Mantis performance for the Microstrip transmission line and the high-pass filter. The case with a HPF installed shows no degradation on the signal to noise performance, and in fact an increase in SNR was recorded. However, it is postulated that the increase in SNR for the HPF case could be due to variability in the physical tamper applied. While not an exhaustive investigation, this measurement does indicate that the that the limiting factor for the SNR in the Mantis system is most likely due to correlation noise, rather than the thermal noise limit. By extension, it appears that the HPF should have limited effect on Mantis sensitivity to tampers, while significantly improving the rejection of interference caused by UMS sensor signals.

Table 3. SNR validation of Mantis System with Cs – 137 Source and HPF vs. baseline case (Microstrip with no Cs – 137 source).

Tamper Location	Microstrip Baseline Mag	Microstrip Tamper Mag	Microstrip SNR	HPF Baseline Mag	HPF Tamper mag	HPF SNR
1m	16	122	17.6dB	12	138	21.2dB
25m	16	56	10.8dB	12	44	11.2dB
49m	16	22	2.8dB	12	26	6.7dB

6.3.2 Adapted Mantis-based Prototype: Initial Findings

With the 3-port network and HPF filter design and testing completed, tests were performed to see if this adapted Mantis-based prototype could achieve the still detect tampers for the full range of the 50-m RG-174 test cable, and if the HPF provided enough isolation such that the SSTDR signals generated by Mantis do not influence the detected spectra at the Pocket MCA.

A block diagram and respective picture of the measurement configuration is shown below in Figure 48 and differs from the nominal testbed setup in Figure 8 only by the addition of the HPF at the Mantis input and the use of a modified resistive divider network as the 3-port interface.

With the addition of the HPF, a modified 3-port network was needed that could provide isolation between the Mantis and MCA system and allow for the Mantis and FEUM frequencies to pass as well as DC in the event that Mantis is connected simultaneously with NGAM and a single-cable UMS sensor type. The isolation between the Mantis and MCA/NGAM is required such that the impedance from the MCA/NGAM does not de-tune the HPF installed at the output of the Mantis system. Also it was found that if no isolation was present, the HPF would shunt to ground all the radiation sensor signals such that the MCA would have no spectrum. For these reasons a simple unmatched TEE will not provide sufficient functionality. A common Wilkinson power divider provides high isolation but will not operate at DC. A standard resistive power divider will function but can be tuned for better isolation between the Mantis and MCA/NGAM ports by removal of the 50ohm resister that couples the Mantis and MCA/NGAM ports together. Therefore a standard resistive power divider was modified by removing the 50-ohm resister that couples the Pocket MCA and Mantis.

For these measurements, the radiation source was again the 13.4 micro-Curie ^{137}Cs described previously. The source-to-detector distance was varied between 0 cm and 3 cm to achieve gross count rates of various magnitudes ranging from 3.6 kcps to 16.9 kcps. Likewise, the shaping time of the amplifier in the FEUM unit was varied between 0.2 µs and 1.2 µs to aid the assessment of whether the frequency content of each sensor pulse has a significant impact on interference and performance. It should be noted that while the NaI spectrometer has a resolution of approximately 12% FWHM (662 keV) when operated in isolation, its resolution degraded to 14% when it was connected to the power divider and the high-pass filter. The cause of this decrease needs further investigation, but one explanation is impedance mismatch between various components.

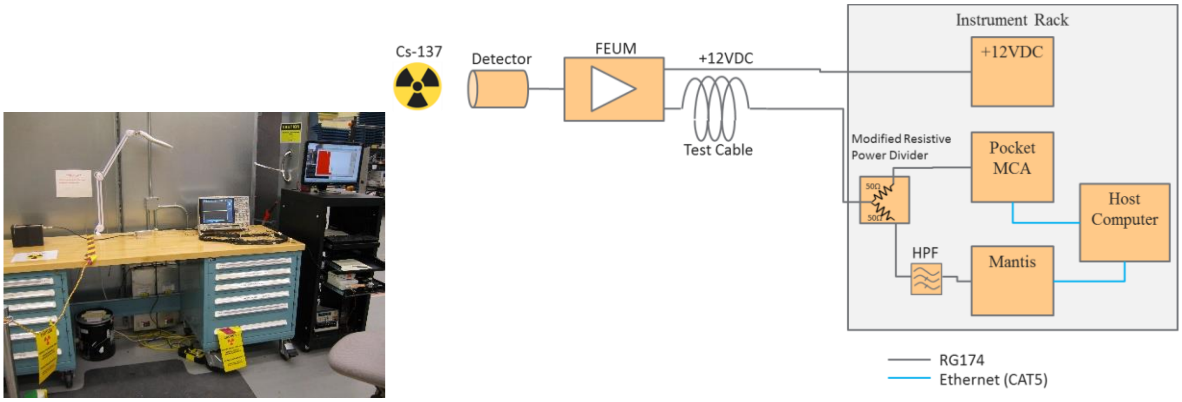

Figure 48. Configuration for the evaluation of the adapted Mantis prototype that includes a 3-port network and HPF.

Table 4 below shows the location, duration and number of tampers at all locations along the 50-m RG-174 test cable. For this measurement study, only a single manual tamper was performed during the collection of a 4-minute Mantis data set. The baseline data set was collected for 10 minutes, without any manual tampers. Note that the baseline performance study described earlier was based on 50 tampers at each location and therefore enabled ROC analysis. Here, the single tamper at each location cannot support a ROC analysis.

Table 4. Tamper measurement study with ^{137}Cs and HPF.

#	Measurement Name	Tamper	# of Tampers	Tamper Duration	Scan Duration
1	TDR baseline	off	0	NA	10mins
2	0m_Tamper	on	1	2 sec	4 min
3	1m_Tamper	on	1	2 sec	4 min
4	5m_Tamper	on	1	2 sec	4 min
5	10m_Tamper	on	1	2 sec	4 min
6	15m_Tamper	on	1	2 sec	4 min
7	20m_Tamper	on	1	2 sec	4 min
8	25m_Tamper	on	1	2 sec	4 min
9	30m_Tamper	on	1	2 sec	4 min
10	35m_Tamper	on	1	2 sec	4 min
11	40m_Tamper	on	1	2 sec	4 min
12	45m_Tamper	on	1	2 sec	4 min
13	49m_Tamper	on	1	2 sec	4 min
14	50m_Tamper	on	1	2 sec	4 min

The measured Mantis data matrices were processed as before with the FFT and BSRA methods. The results for the no-tamper baseline measurement with the presence of the ^{137}Cs source are shown in Figure **49**, on a logarithmic scale to highlight the small occurrences. Consistent with the no-tamper baseline shown in Section 6.3, without the HPF and resistive divider, the range of the signal amplitudes is +/- 7.325 in. In this case, however, this relatively tight distribution on the system noise was achieved in the presence of a relatively high UMS sensor count rate.

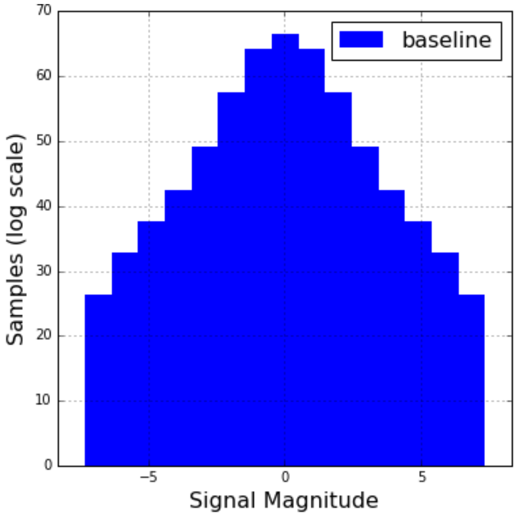

Figure 49. Histogram of processed Mantis data with 3-port network, HPF and ^{137}Cs source and no tampers present.

Figure 50 shows the processed (FFT and BSRA) Mantis data matrix for a few-second subset of the 4-minute acquisition during which a tamper was applied at 49 m. Even in the presence of the high sensor count rate, the tampers are readily recognized.

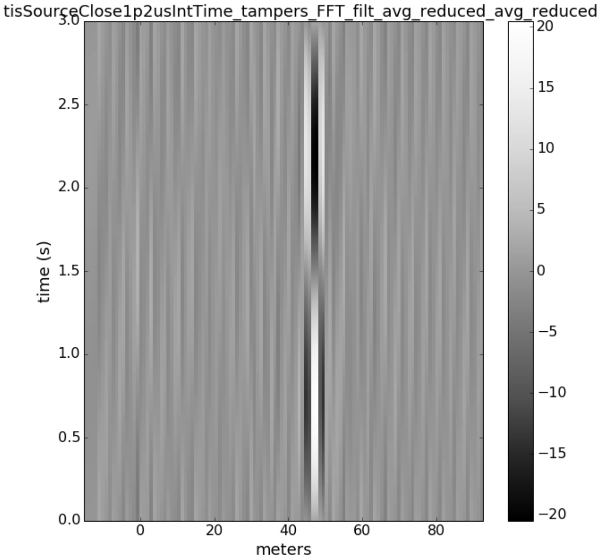

Figure 50. Measured Mantis data matrix, processed using FFT and BSRA, with HPF, divider network and high count rates on the NaI sensor. The presence of a few-second long tamper at 49m is clear.

As in previous analyses, the maximum event amplitudes for each tamper and the noise baseline were used to calculate SNR. Note that the SNR is calculated by:

$$SNR = 20\log_{10}(Tamper\_magnitude/Baseline\_magnitude)$$

A summary of the measured SNR for tampers at different locations, with a NaI count rate of 16.9 kcps and a shaping time of 1.2μs, is given in Table 5. These data are represented graphically in Figure 51.

Table 5. Measured signal to noise ratio for tampers installed with the presence of a ^{137}Cs source.

#	Measurement Name	Magnitude (+/-)	SNR (dB)
1	TDR baseline	7.3	NA
2	0m_Tamper	661	39.1
3	1m_Tamper	62	18.6
4	5m_Tamper	59.7	18.3
5	10m_Tamper	56	17.7
6	15m_Tamper	46	16.0
7	20m_Tamper	36	13.9
8	25m_Tamper	1047	43.1
9	30m_Tamper	25.7	10.9
10	35m_Tamper	19.5	8.5
11	40m_Tamper	18	7.8
12	45m_Tamper	14.1	5.7
13	49m_Tamper	20.5	9.0
14	50m_Tamper	23.9	10.3

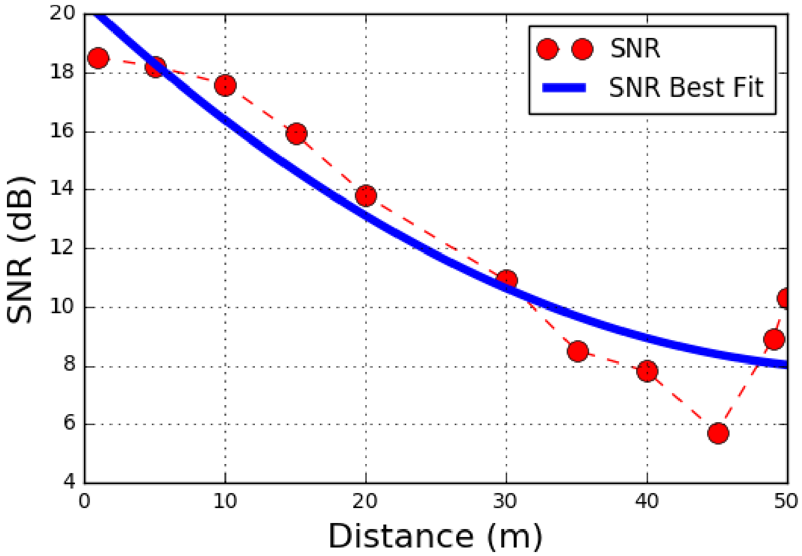

Figure 51. Tamper SNR versus distance concurrent with a NaI count rate of approximately 17 kcps.

It is important to note that the tamper at 25m with a very large amplitude is most likely due to an accidental shorting of the probe to the outer conductor while in contact with the center conductor as this will produce a very large response. While highlighting the possibility of a tamper to short circuit the coaxial cable during the tamper process, this also poses the need for repeatable tampering in order to produce good statistics and reject outliers that are due to inconsistent tampering; this is discussed in future work.

6.3.3 Effect of Mantis on Radiation Sensor Signals

The Mantis system, utilized for TDR measurements, injects a low-power signal over a wide frequency range into the test cable that also carries the signal originating from a radiation detector. Without proper signal filtering, it is very likely that the detector signal undergoes distortion or degradation due to interference with the Mantis SSTDR signal. Figure 48 also depicts the test configuration for these tests, in which the pocket MCA spectra were used to quantify whether Mantis SSTDR signals cause any distortion on the radiation-sensor signal. In order to measure the effect of Mantis on the sensor signal, a series of gamma-ray spectra at various operating conditions were measured, as described in Table 6 and the text below.

Table 6. Test parameters for analysis of Mantis interference on NaI spectrometer signals.

Measurement Type	**Amplifier Shaping Time (μs)**
Baseline, Source only	1.2
Mantis, Source	1.2
Mantis, Source, Tampers	1.2
Baseline, Source only	0.2
Mantis, Source	0.2
Mantis, Source, Tampers	0.2

Source only: A ^{137}Cs gamma-ray spectrum measured while the Mantis system is *inactive.*

Mantis, Source: A ^{137}Cs gamma-ray spectrum measured while the Mantis system is *active.*

Mantis, Source, Tampers: Physical tamper and signal tapping conducted on the test cable while a ^{137}Cs gamma-ray spectrum is measured and the Mantis system is active.

The gamma-ray spectrum will exhibit the Mantis interference signature in one or more of the following ways:

- Artifact (extra peaks, for example) in the spectrum for which the origin is not from gamma radiation;
- Increase in photopeak FWHM;
- Photopeak centroid shift;
- High dead-time.

Example spectra for the various testing combinations are shown in the figures below; quantitative results are tabulated in Table 7.

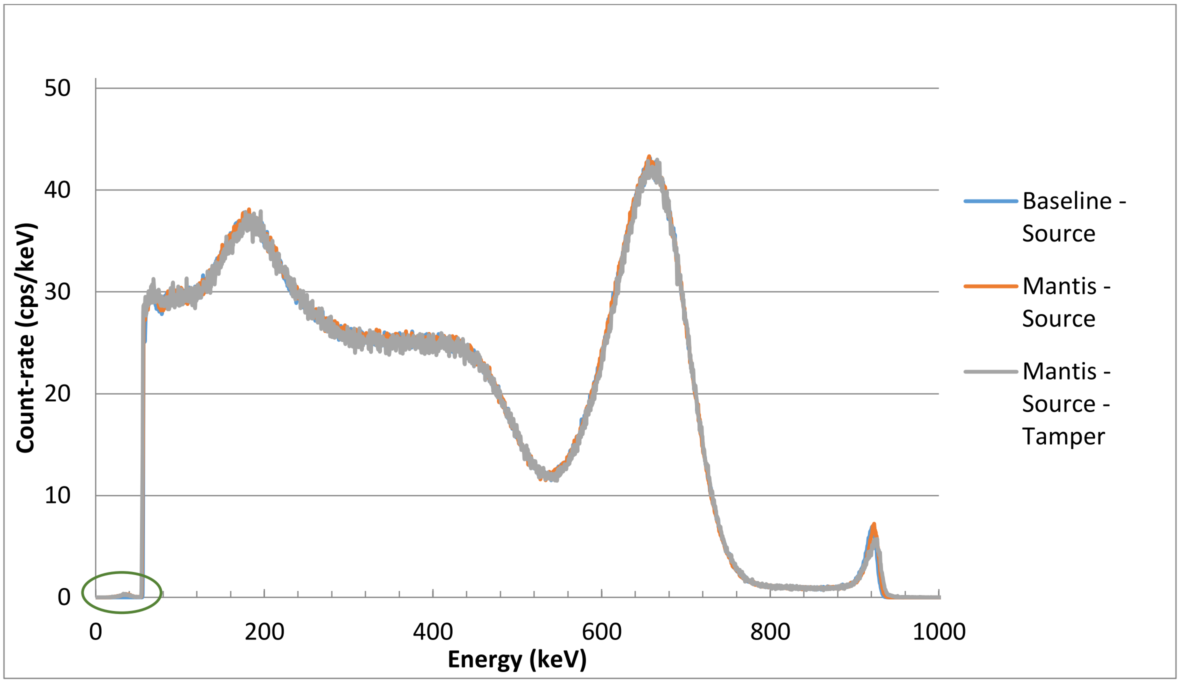

Figure 52. Gamma-ray spectra at 1.2 μs shaping time

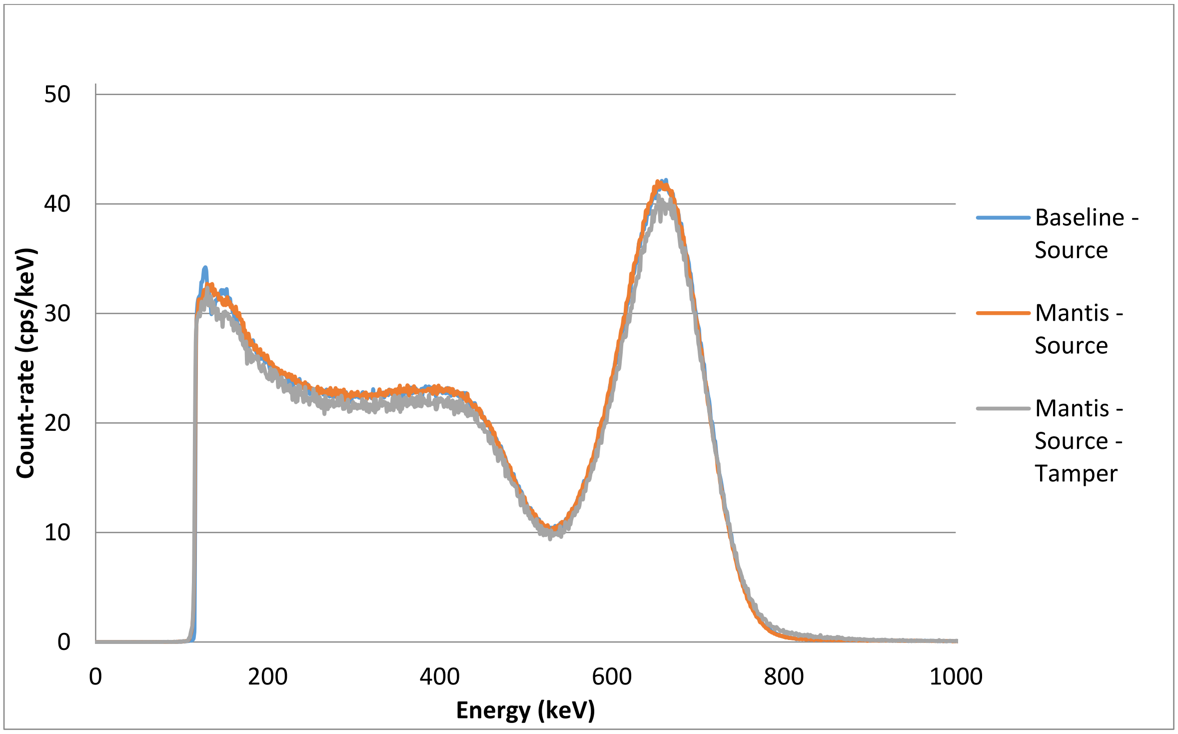

Figure 53. Gamma-ray spectra at 0.2 μs shaping time.

Table 7. Quantitative summary of Mantis effects on signals from a NaI sensor.

Measurement Type	τ (μs)	Centroid (ch)	Δ Centroid (%)	FWHM (keV)	Δ FWHM (%)
Baseline, Source only	1.2	1376.47	0.0	14.1	0.0
Mantis, Source	1.2	1378.81	0.2	14.2	1.2
Mantis, Source, Tampers	1.2	1392.01	1.1	14.4	2.6
Baseline, Source only	0.2	672.36	0.0	16.2	0.0
Mantis, Source	0.2	673.53	0.2	15.6	-3.6
Mantis, Source, Tampers	0.2	676.08	0.6	16.1	-0.5

Overall, the results show that interference from Mantis on gamma-ray spectra is insignificant—the relative changes in the centroid locations and FWHM are quite low. The FWHM at faster shaping time (τ = 0.2 μs) is marginally higher as compared to a slower shaping time (τ = 1.2 μs), as would be the case without Mantis (due to ballistic deficit effects). This minimal impact can be explained by the fact that the Mantis SSTDR signal presented to the MCA consists of relatively low-amplitude, high-frequency content that adds a bit of random noise on a pulse-by-pulse basis, but in aggregate, has no noticeable effect.

6.4 Prototype Testing Configuration: Summary

For reference, the latest configuration of the laboratory prototype TI module and associated testbed, for both hardware and software, is listed below.

- Hardware Configuration:
  - Sealed Source: 13.4 microCi ^{137}Cs
  - FEUM settings: gain stage 1 = B, gain stage 2 = 6, shaping time = 1.2us
  - Cable under test: 50m RG174, 50-ohm coaxial cable
  - 3-port network: resistive power divider with open circuit between MCA and Mantis ports
  - External HPF cutoff frequency: 5MHz
- Software Configuration:
  - Digital FFT low pass filter cutoff frequency: 0.25Hz
  - Baseline signal subtracted, average value in time and distance dimension removed (BSAR)
- Mantis Configuration:
  - SSTDR frequency: 24MHz
  - Amplitude: 132mVpp
  - Pseudo noise code length: 160us
  - Output file format: raw .lwi data

7.0 Supporting Hardware Developments

In parallel with the measurement studies and single-channel prototype adaptations described above, PNNL has also pursued hardware and software developments intended to further evolve the concept of TDR for UMS applications, and to facilitate efficient and effective testing of prototype instruments in FY17.

7.1 Multiplexing: Single Mantis for Multiple Cables

The concept of multiplexing through additional cables was proposed in order to monitor up to 8 individual coaxial cables with a single Mantis system. This capability is likely to be an important implementation cost/complexity factor for IAEA UMS systems that often have multiple cables. There are many low cost commercially available solutions for radio – frequency (RF) switches that will connect a single input (the common port) to many outputs. The standard description for these switches is single pin, *n* – throws, where *n* is the number of output ports. Note that these switches are reciprocal in that they allow the signal to pass through both directions.

A switch was selected from Analog Devices, part number HMC322ALP4E, which operates from DC – 8GHz--easily encompassing the frequency range of the Mantis system. These switches are surface-mount components that can be installed on a printed circuit board (PCB). The switch was purchased on an evaluation PCB for $500 to reduce initial engineering development costs and enable more rapid adoption into PNNL’s TDR testbed. For future field prototype designs, the surface-mount component could be purchased at $100 / switch, allowing Mantis to toggle between 8 cables. Figure 554 below shows the switch labeled with U1, and its associated RF ports. The switch is controlled using transistor – transistor logic (TTL) that has a 5VDC delta between logic states. There are three logic pins that are controlled using TTL: A, B, and C. The voltage levels applied to the logic pins determine the RF path, RF common to RF port #.

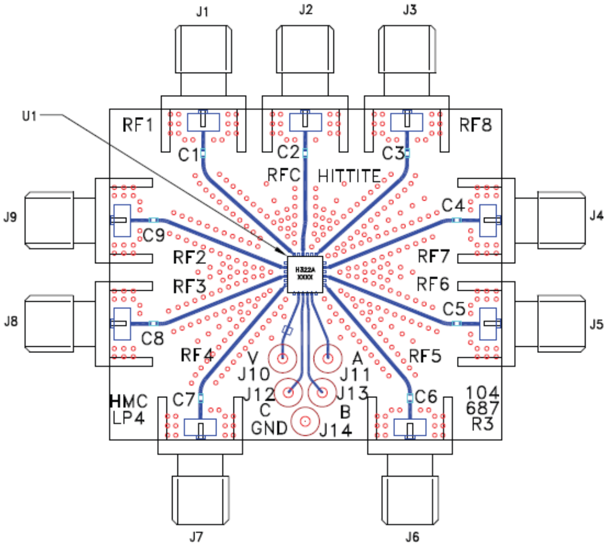

Figure 54. Analog devices evaluation PCB for HMC322ALP4E.

Three waveform generators were connected and synchronized in time in order to sequence through the 8 logic states with the three logic pins. Figure 55 below is a screen capture on an oscilloscope of the square waveforms used to drive the logic pins into their respective logic states. In a deployed system, the logic pin could be easily controlled with a microcontroller or embedded system, the use of the three function generators was simply a proof-of-concept measurement.

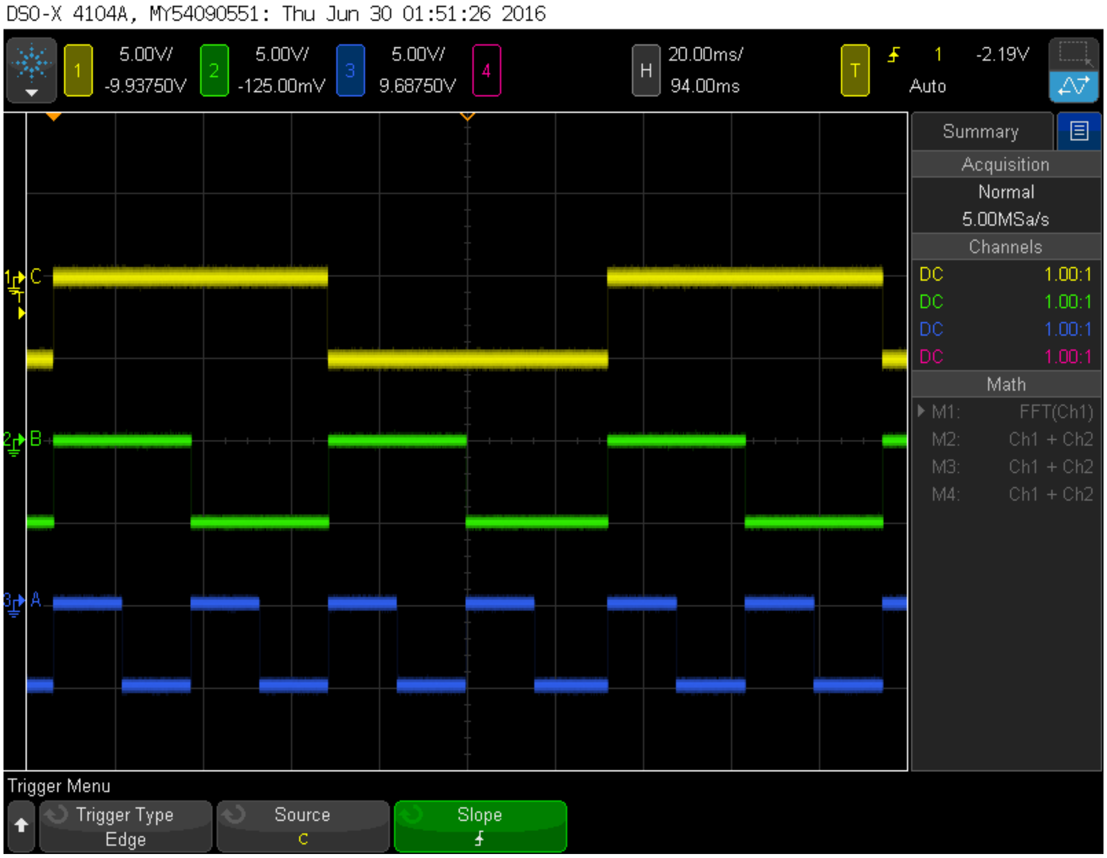
DSO-X 4104A, MY54090551: Thu Jun 30 01:51:26 2016

Figure 55. Measured TTL waveforms on oscilloscope for controlling multiplexing switch logic.

The measurement configuration for testing the viability of Mantis multiplexing between cables was Mantis connected to the switch common port; the 8 ports of the switch were all connected to RG-174 cables. Each RG-174 cable was left with an open circuit at the end, and they were all different lengths from each other. This allowed for readily observing the sequencing through the cables in the resulting Mantis data. The test configuration and initial measurement results are shown below in Figure 56.

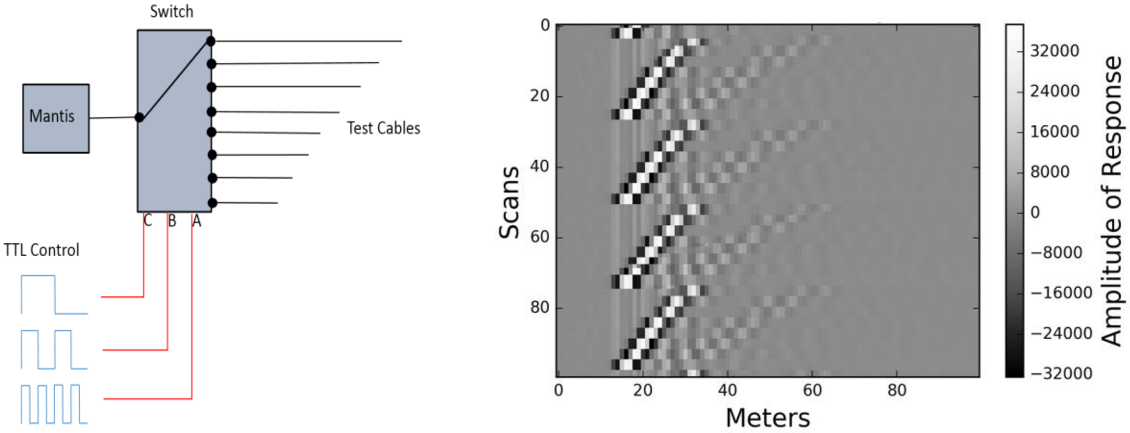

Figure 56. Block diagram of Mantis multiplexing (left) and measured SSTDR output (right).

In this test configuration the Mantis SSTDR measurement is not synchronized in time with the switching of the cables, which creates some level of distortion/misalignment when sequencing through the cables under test. However, the proof-of-concept measurements demonstrate that this RF switch can be used to multiplex Mantis through multiple cables. Future work will include coordination of timing between the SSTDR measurement and the switch. Prior investigation revealed that LiveWire's ASIC has a BUSY pin (Figure 57), which is high for the duration of a scan and goes low between scan times, that could support the necessary synchronization. PNNL is currently investigating whether Mantis has a similar functionality.

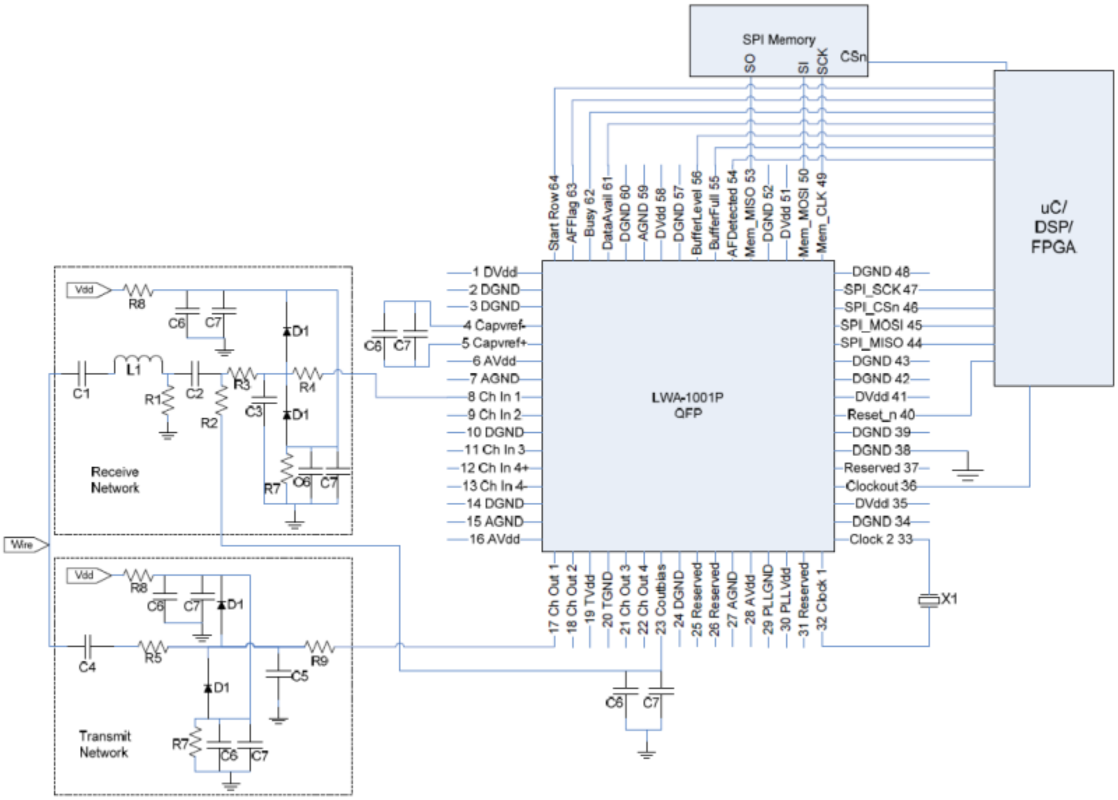

Figure 57. Pinout of LiveWire's SSTDR ASIC, showing busy pin that could support switch sequencing.

7.2 Benchtop Apparatus for Automated Tampering

In order to improve the repeatability of tampers and reduce the manual burden of physically tampering many times at various distances, PNNL has developed an automated tool to insert the oscilloscope probe into the cable under test. The design uses a stepper motor and guide-rail system to precisely move the attached oscilloscope probe in and out of the tamper in the cable. Using a Python script, the pressure, duration and rate of tampering can be controlled. In the future, the device will also use the signal measurements on the oscilloscope produced by the probe tampering to validate if the tamper achieved good contact. This quality-control feature will become increasingly important as large measurement data sets are automated. The goal of this instrumentation is to provide the ability to produce large tamper data sets to support high-precision ROC curves, and highly reproducible tamper parameters such as pressure, duration and rate.

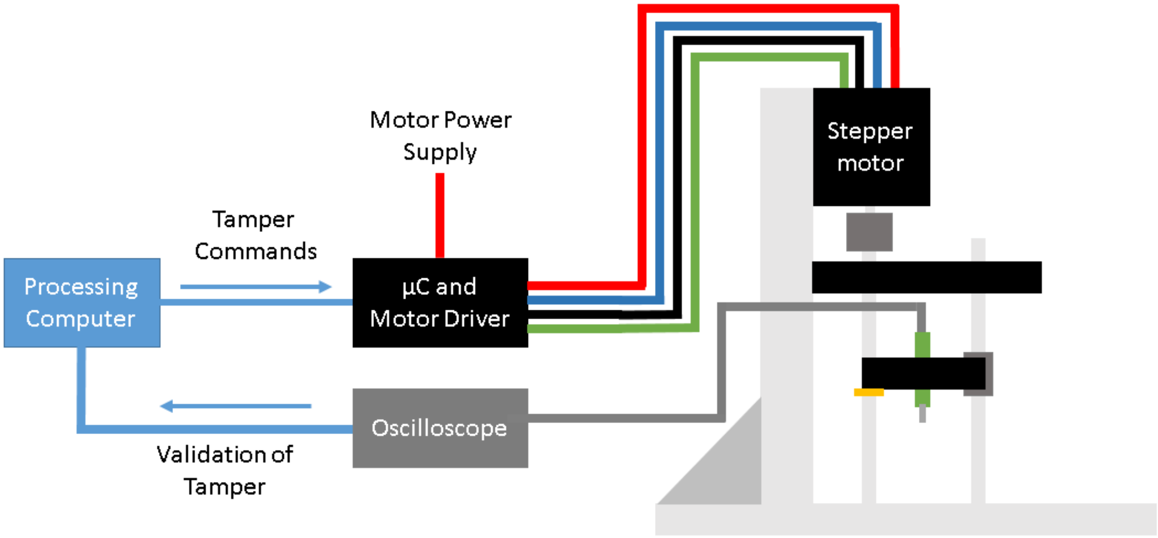

Figure 58. Automated tamper implementation and validation setup.

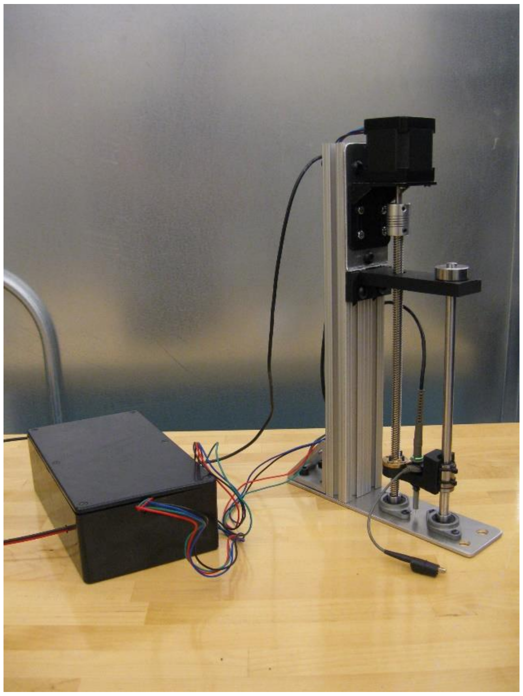

Figure 59. Automated tamper prototype.

7.3 Graphical User Interface Development

PNNL has begun to develop a graphical user interface (GUI) for dynamically changing processing parameters during monitoring. This means that while a large data set is being processed, the user can change the processing parameters and optimize values such as FFT frequency cutoff, Import class window size, Import class window overlap, and threshold. This allows the user to tune the detection algorithms in real time to the cable environment to reduce noise and highlight any artifacts.

This GUI is currently in development, and could be used to support real-time data being streamed from the Mantis system, flagging tampers according to measurement settings and outputting comma separated value files with the time a tamper occurred, location and amplitude. The goal of this GUI is to provide a simple user interface to the Mantis system that will take advantage of the Mantis hardware and PNNL developed software.

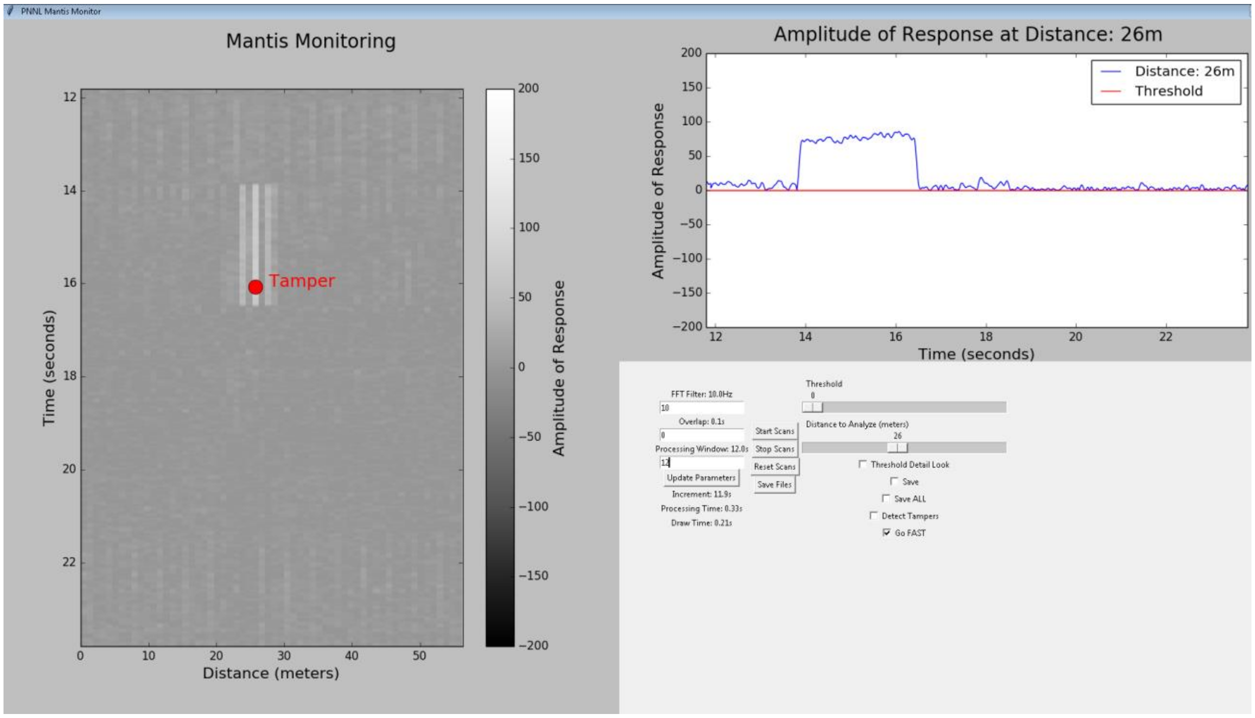

FFT Filter: 10.0Hz
10
Overlap: 0.1s
0
Processing Window: 12.0s
12
Increment: 11.9s
Processing Time: 0.33s
Draw Time: 0.21s

Threshold
0
Distance to Analyze (meters)
26
☐ Threshold Detail Look
☐ Save
☐ Save ALL
☐ Detect Tampers
☑ Go FAST

Figure 60. Screenshot of Mantis Monitor GUI, showing the results for a tamper at a start time of approximately 16 seconds.

8.0 Conclusions

The key technical questions that guide this viability study, and the findings derived from the FY16 work performed by PNNL (measurement studies, signal processing techniques, statistical analysis and hardware development) are summarized here.

1) Can active TDR signals be distinct/separable from the frequency spectra of UMS sensors?

The preliminary findings is that Mantis SSTDR signals are largely distinct from UMS radiation-sensor signals in terms of frequency content, but there is sufficient overlap that interference is observed. UMS signals have very low-frequency content, typically less than 3MHz. The SSTDR signal generated by the Mantis system covers a broad frequency range from low KHz up to 5 times the modulation frequency. For this measurement study the SSTDR frequency range was nominally 5KHz -120 MHz. As previously discussed Mantis utilizes an SSTDR BPSK approach which effectively encodes a waveform, by phase shifting it with a known but random sequence. As a waveform is encoded in this manner, it spreads the energy that is typically encompassed in a single frequency over a wide frequency range. This makes the Mantis system have very small amounts of energy over a wide bandwidth instead of a large signal amplitude at a single frequency. The encoded waveform allows for comparison, or correlation, to a reference signal which provides processing gain to extract the SSTDR signal from the noise or other potential interfering signals. It was observed that even though the UMS radiation sensor pulses do not correlate well with the SSTDR reference signal, they still produce a noise structure that can mask certain types of tamper responses. Therefore, suitable combinations of hardware filtering (e.g., a HPF at the Mantis input) and digital signal processing are needed to enable Mantis and UMS sensor to coexist. It should be noted that the FY16 findings regarding Mantis and UMS sensor interference are based on the relatively large-amplitude, analog bipolar pulses produced by a NaI(Tl) spectrometer. Other common UMS signal types, including smaller analog signals typical of room-temperature semiconductor detectors, and TTL signals, need quantitative study.

2) How effectively can candidate methods (hardware + algorithms) detect tampering scenarios?

For all of the cases tested to date, the Mantis SSTDR interrogation, in conjunction with PNNL’s HPF and application-specific digital signal processing algorithms, were able to detect tampers at all locations along the 50m RG-174 test cable. This preliminary capability demonstration was based on a subset of the common UMS use parameters (i.e., cable type, tamper type, UMS sensor signal and count rate, etc.); further study of other implementation parameters, including cables to 200m in length, RG-71 cable and different UMS signal types (see above) is needed to more fully characterize the tamper-detection performance for IAEA implementation scenarios.

3) How might an active TDR device interface with common IAEA data acquisition systems?

The Mantis system is a self-contained unit designed to easily connect to a host computer via Ethernet or Wifi, but the standard operating mode, which does not support collection of raw data and has alarm algorithms designed for very large impedance changes, is not well-aligned with IAEA use cases. For the IAEA, collection of raw data and subsequent (possibly real-time but at least post-processing) analysis using IAEA-specific signal processing and alarm algorithms will be necessary to realize the Mantis potential for tamper-indication on cabling. Adaptations of Mantis firmware, and specialized analysis algorithms, are needed to meet IAEA’s UMS needs. FY16 work provided proof-of-concept for these adaptations; further refinement and tested are needed.

4) Are there obvious vulnerabilities in the methods and, if so, how might they be addressed?

While the FY16 scope has shed encouraging light on the potential of Mantis for IAEA UMS applications, there has been no concerted effort to assess or mitigate potential vulnerabilities. Guidance from the IAEA is needed to define the parameters and boundary conditions of a vulnerability study, and such a study would be the subject of future work. The Mantis system in conjunction with PNNL’s signal processing algorithms and external HPF has demonstrated the ability to detect all physical tampers tested from 0 to 50m on a RG-174 coaxial cable. With regards to physical tampering, disconnects, splices there are no known vulnerabilities at this time. The Mantis SSTDR does not address the potential of a non-contact listen and playback method. There may be the possibility of state of the art real time spectrum analysis to measure the leaked RF signals from cable shielding due to the braided nature of the RG-174 outer conductor. The braided outer conductor is not as effective as a solid conductor at shielding the coaxial cable line from being listened to or interfered with. Mantis is designed to detect impedance changes and a non-contact system would not present an observable impedance change to Mantis.

9.0 Future Work

PNNL's recommendations for the continuing investigation of Mantis viability for IAEA UMS applications are given below:

1) Complete ROC analysis for initial test case (i.e., 50-m RG-174) using the new automated cable tampering capability, then extend that analysis to include test cases suggested by the IAEA (status meeting in Vienna, October 2016), for example: smaller analog signals on cables to 200m in length; NGAM data acquisition; TTL signal at various rates and pulse widths; RG-71 cabling; and consideration of nonintrusive taps.

2) Demonstrate proof-of-concept cable multiplexing: Typical IAEA UMS systems include multiple cables, often up to eight, for each data acquisition system. Devoting a Mantis system to each cable would not be cost-effective (at ~$5k per Mantis module). The cost and footprint associated with monitoring multiple cables at a time can be greatly reduced by time sequencing and multiplexing between cables with one Mantis system. PNNL will continue its development of a proof-of-concept multiplexer prototype based on COTS components, and demonstrate that the device will work hand in hand with the Mantis system, PNNL detection algorithms, high pass filter, and data acquisition electronics.

3) Perform harsh-environment testing: The primary focus of FY16 work was to determine the sensitivity of the Mantis system to small impedance changes on a cable line, determine its location accuracy, and develop detection algorithms to increase sensitivity post data collection. Toward increasing realism, a testing effort is proposed to present a modified noise floor scenario to the hardware settings and algorithms developed in FY16, to assess performance, determine gaps and make necessary adjustments. The modified noise floor will be achieved by presenting gross changes to the cable under test that are common to industrial environments, such as high levels of external electromagnetic interference as presented in an anechoic chamber. Modifications to the cable environment are expected to increase noise levels through the preprocessing algorithms and thus require additional signal processing techniques to overcome the noise and maintain required sensitivity to detect physical tampers at distances of concern.

4) Signal Processing Algorithms: The custom signal processing algorithms designed by PNNL are currently written for standard laboratory computing hardware. PNNL will adapt the software to support the high-priority implementation modes envisioned by the IAEA, with the initial priority being the post-processing of raw data at IAEA headquarters by the Remote Monitoring Team. The need for other modes, for example near-real-time monitoring in the local data acquisition cabinet, will also be discussed with the IAEA. PNNL will continue to work under the model of nonproprietary software that can be openly shared with the IAEA. .

5) Field testing: Building on the lessons learned from testing of the laboratory prototype, PNNL will work with the IAEA to define and execute a long-term test in a representative facility. The Mantis system will be operated with determined hardware configurations, and PNNL-developed signal processing algorithms will be used to assess expected performance in the presence of noise and cable structure of an actual facility.

10.0 References

[1] Smith LE, Svoboda J, Ianakiev K, et al. 2014. “Front-end electronics for verification measurements: performance evaluation and viability of advanced tamper indicating measures." IAEA International Safeguards Symposium.

[2] Smith LE, P Ramuhalli, DM Sheen, JR Tedeschi, RC Conrad, K Ianakiev, M Browne, J Svoboda, J West and J Sanders. 2014. Detection of Physical Intrusion in the Cabling of Unattended Safeguards Instruments: Preliminary Requirements and Evaluation Scenarios. PNNL-23749, Pacific Northwest National Laboratory, Richland, Washington.

[3] Keysight Technologies. 2014. Keysight Electronic Calibration (ECal) Modules for Vector Network Analyzers - Technical Overview. Keysight Technologies, Inc. Santa Rose, California. Accessed November 11, 2014. Available at http://literature.cdn.keysight.com/litweb/pdf/5963-3743E.pdf.

[4] Agilent. 2012. Time Domain Analysis Using a Network Analyzer. Application Note 1287-12, Agilent Technologies, Santa Clara, California. Available at http://cp.literature.agilent.com/litweb/pdf/5989-5723EN.pdf.

[5] Wadell BC. 1991. "Transmission Line Handbook" Norwood, MA: Artech House Inc.

[6] LiveWire. 2014. Live Cable Fault Monitoring. LiveWire Innovation. South Jordan, Utah. Accessed November 11, 2014. http://LiveWireinnovation.com/.

[7] Smith P, C Furse and J Gunther. 2005. "Analysis of Spread Spectrum Time Domain Reflectometry for Wire Fault Location." IEEE Sensors Journal 5(6):1469-1478.

[8] Tedeschi JR, Smith LE, Moore DE, Sheen DM, Conrad RC, Gavric G. Active Time-Domain Reflectometry for Unattended Safeguards Systems: FY15 Report. PNNL – 24726, Pacific Northwest National Laboratory, Richland, Washington.

[9] Conrad RC, Keller D, Morris SJ, Smith LE, “Front-end Electronics for Unattended Measurement (FEUM): Results of Prototype Evaluation,” PNNL-SA-24552, Pacific Northwest National Laboratory, Richland, WA, August 2015.

[10] Conrad RC, Keller D, Morris SJ, Smith LE, “Front-end Electronics for Unattended Measurement (FEUM): Prototype Test Plan,” PNNL-24553, Pacific Northwest National Laboratory, Richland, WA, August 2015.

[11]Mosteller, F. and Tukey, J. W. (1977) Data Analysis and Regression. Reading, MA: Addison-Wesley.

[12] JP Proakis, DG Manolakis, Digital Signal Processing, Principles, Algorithms and Applications (4th Edition)

[13] B Gold, AV Oppenheim, CM Rader, Theory and Implementation of the Discrete Hilbert Transform, MIT 1969.

Appendix A

ROC Curves for Tamper Measurement Study Phase II

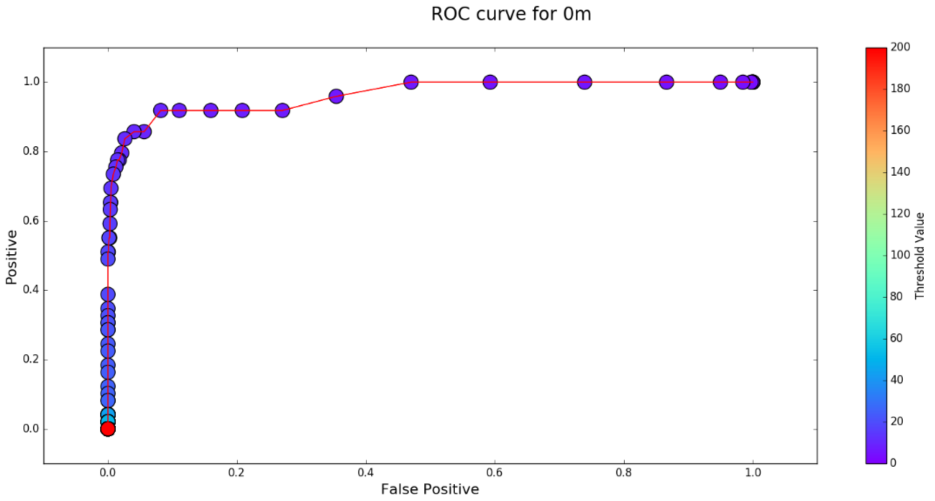
ROC curve for 0m
Positive
False Positive
0.0
0.2
0.4
0.6
0.8
1.0
Threshold Value
0
20
40
60
80
100
120
140
160
180
200

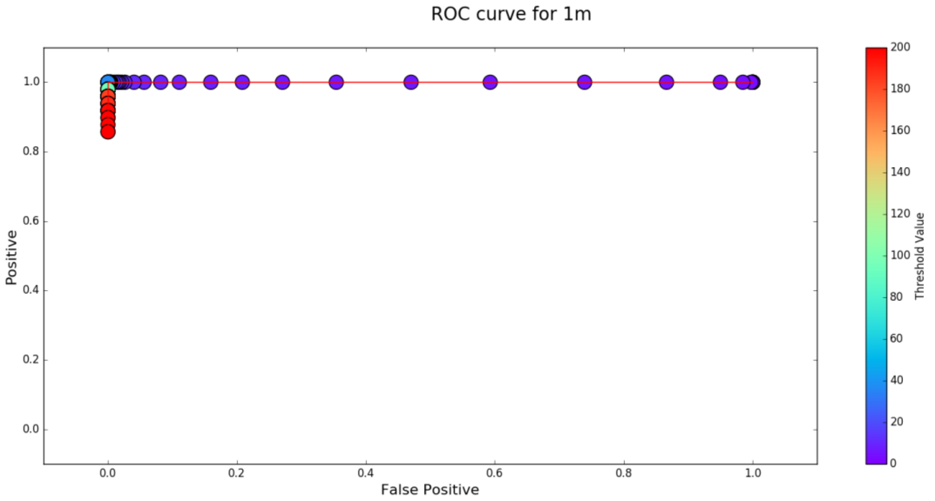
ROC curve for 1m
Positive
False Positive
0.0
0.2
0.4
0.6
0.8
1.0
Threshold Value
0
20
40
60
80
100
120
140
160
180
200

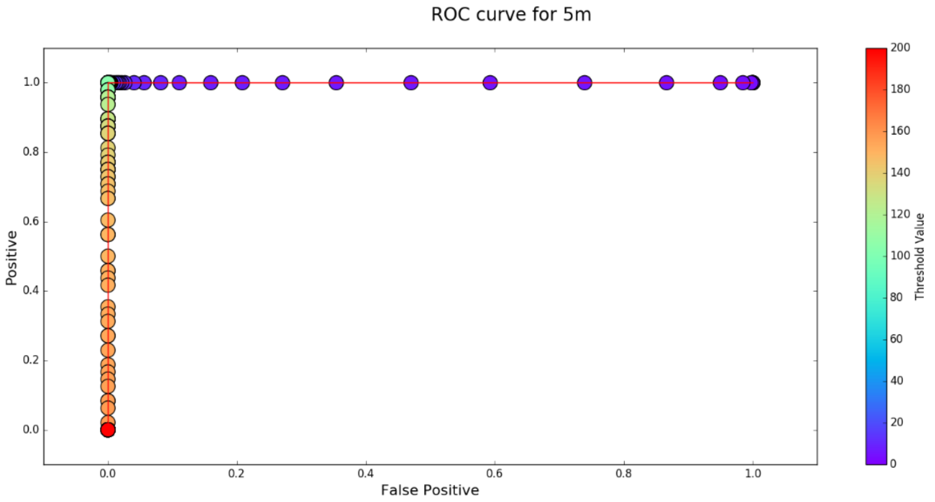
ROC curve for 5m
Positive
False Positive
0.0
0.2
0.4
0.6
0.8
1.0
Threshold Value
0
20
40
60
80
100
120
140
160
180
200

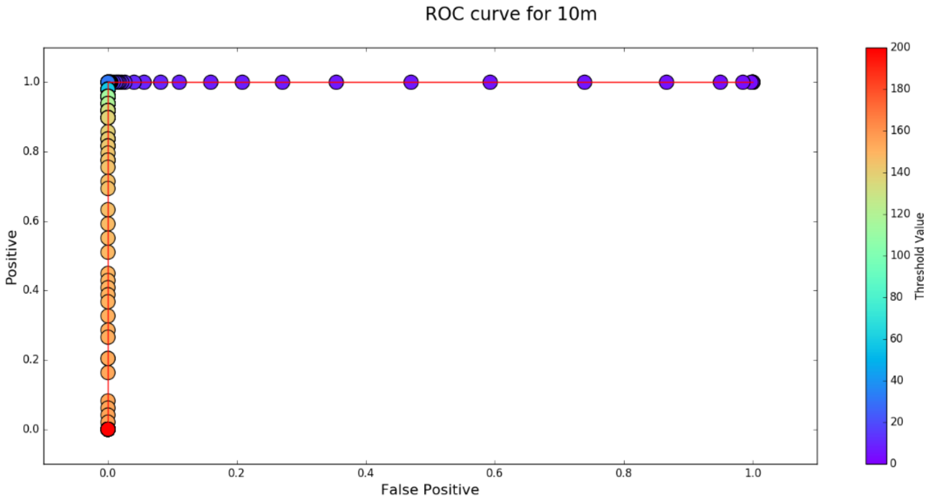
ROC curve for 10m
Positive
False Positive
0.0
0.2
0.4
0.6
0.8
1.0
Threshold Value
0
20
40
60
80
100
120
140
160
180
200

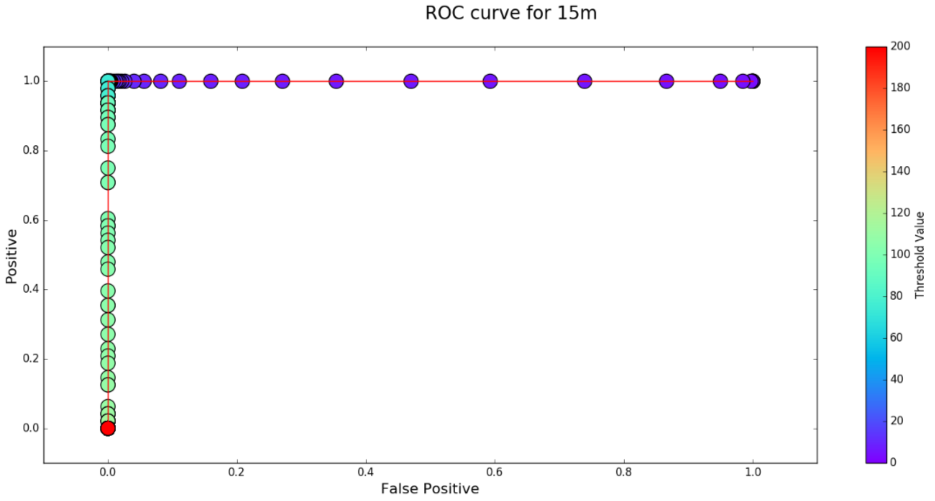
ROC curve for 15m
Positive
False Positive
0.0
0.2
0.4
0.6
0.8
1.0
Threshold Value
0
20
40
60
80
100
120
140
160
180
200

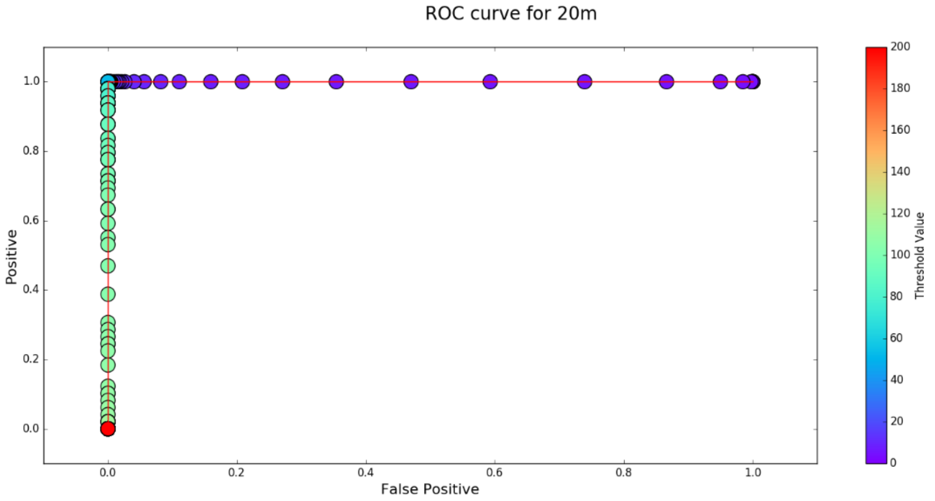
ROC curve for 20m
Positive
False Positive
0.0
0.2
0.4
0.6
0.8
1.0
Threshold Value
0
20
40
60
80
100
120
140
160
180
200

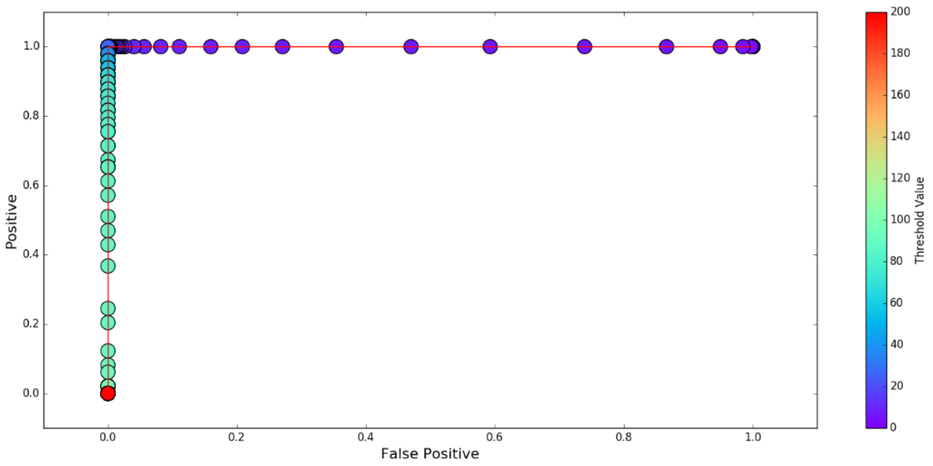

ROC curve for 25m

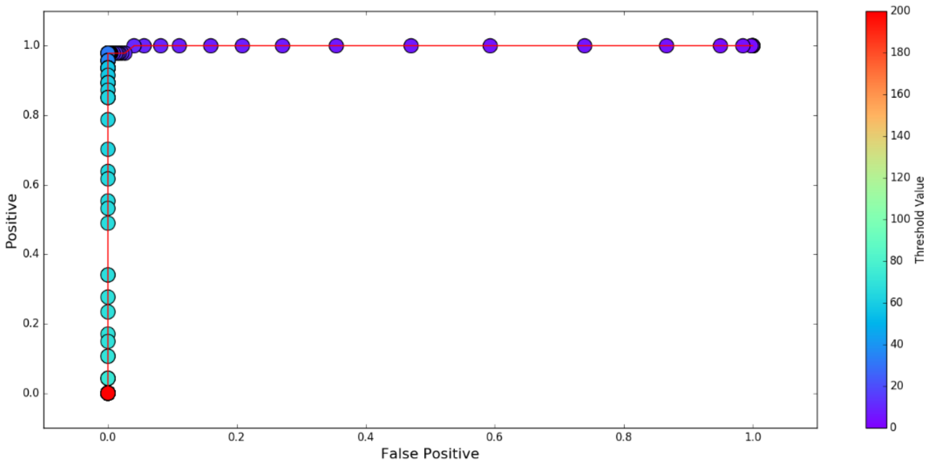

ROC curve for 30m

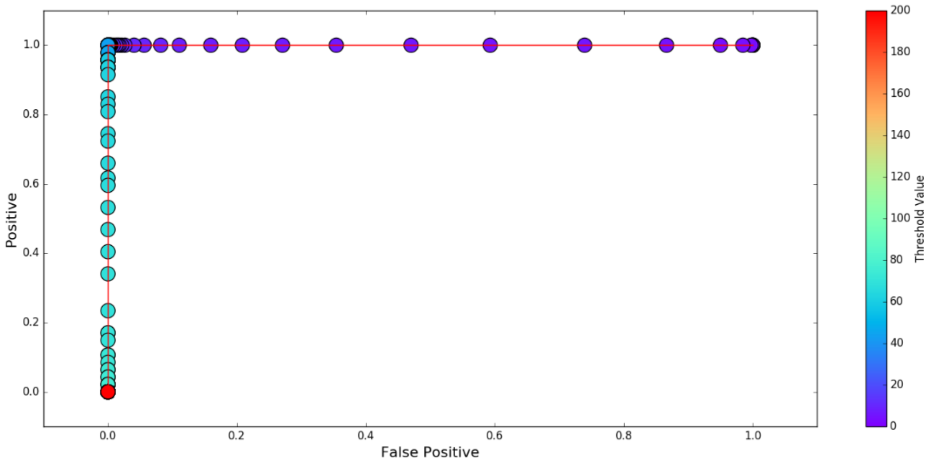

ROC curve for 35m

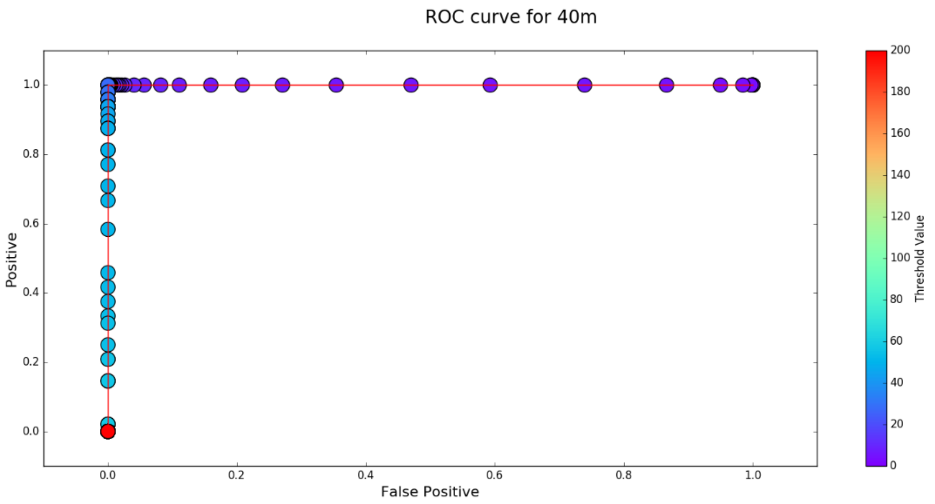
ROC curve for 40m
Positive
False Positive
0.0
0.2
0.4
0.6
0.8
1.0
Threshold Value
0
20
40
60
80
100
120
140
160
180
200

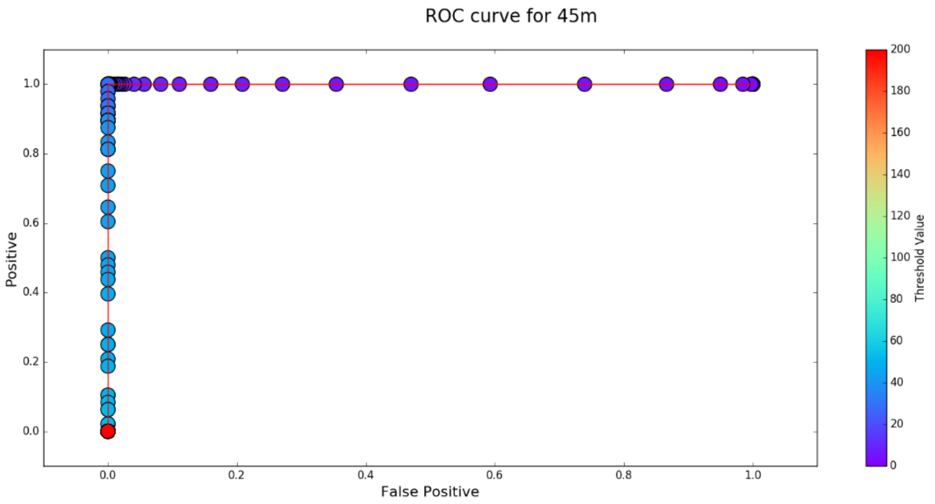
ROC curve for 45m
Positive
False Positive
0.0
0.2
0.4
0.6
0.8
1.0
Threshold Value
0
20
40
60
80
100
120
140
160
180
200

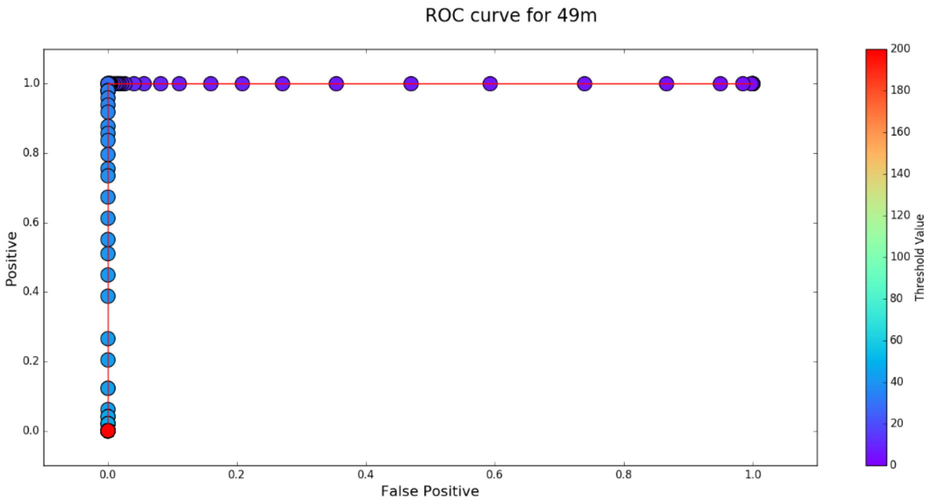
ROC curve for 49m
Positive
False Positive
0.0
0.2
0.4
0.6
0.8
1.0
Threshold Value
0
20
40
60
80
100
120
140
160
180
200

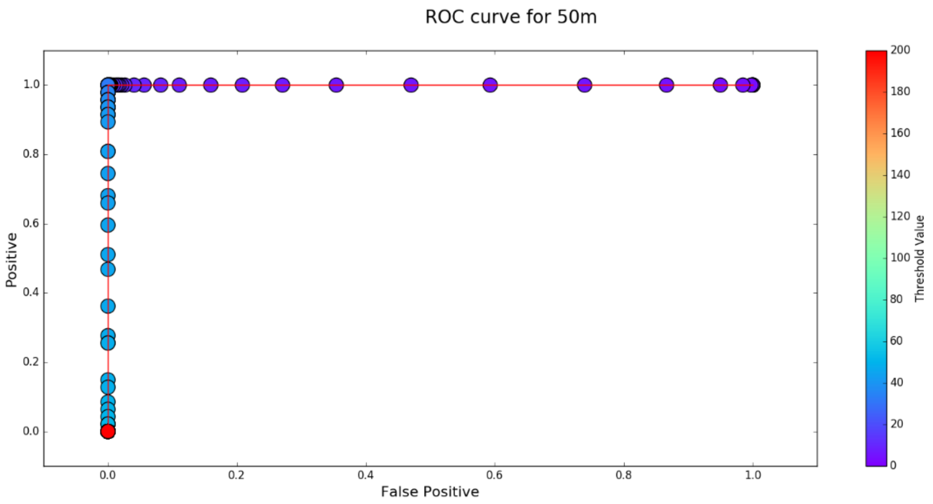
ROC curve for 50m
Positive
False Positive
1.0
0.8
0.6
0.4
0.2
0.0
0.0
0.2
0.4
0.6
0.8
1.0
Threshold Value
200
180
160
140
120
100
80
60
40
20
0

www.pnnl.gov

Pacific Northwest
NATIONAL LABORATORY
Proudly Operated by **Battelle** *Since 1965*

U.S. DEPARTMENT OF
ENERGY

902 Battelle Boulevard
P.O. Box 999
Richland, WA 99352
1-888-375-PNNL (7665)